Department of Physics and Astronomy
University of Heidelberg

Bachelor Thesis in Physics
submitted by

Constantin Schuster

born in Worms (Germany)

2018

Darkfield Microscopy on plasmonic Nanostructures

This Bachelor Thesis has been carried out by Constantin Schuster at the
Kirchhoff Institute for Physics in Heidelberg
under the supervision of
Prof. Dr. Na Liu

Abstract

Dark field microscopes allow only scattered light to enter the objective. This means, that only very little direct light from the source makes it into the resulting image, creating a dark, almost black background behind the brightly lit scattering features of the sample under the microscope. Due to direct light from the light source being almost completely excluded in the final image, dark field spectroscopy is ideal to make extremely small structures well visible. It can be used to make individual particles only a few hundred nanometers in diameter visible via optical microscopy, and even allows for spectroscopy on a single particle. The setup of a dark field microscope, as well as its calibration and first measurements, were at the center of this thesis. The function of a dark field microscope will be explained, and the experimental results will be shown.

Zusammenfassung

Bei der Dunkelfeldmikroskopie werden spezielle optische Elemente benutzt, um zu vermeiden, dass das Licht der Lichtquelle direkt das Objektiv erreicht. Stattdessen wird nur das von der Probe gestreute Licht vom Objektiv eingefangen. Dies erzeugt einen dunklen, fast schwarzen Hintergrund, vor dem die streuenden Strukturen der beobachteten Probe hell leuchtend sichtbar sind. Dadurch können auch sehr kleine Strukturen nachgewiesen werden, die mit ihrer Größe unter dem Beugungslimit liegen. Dunkelfeldmikroskopie kann auch dazu verwendet werden, spektroskopische Untersuchungen an solch kleinen Partikeln durchzuführen, was sie für die Nanotechnologie besonders interessant macht. Im Zentrum dieser Arbeit war der Aufbau eines solchen Mikroskops, und erste Messungen zur Kalibrierung des Aufbaus werden in dieser Arbeit vorgestellt.

Contents

1 Introduction

In recent decades, nanotechnology has grown from a niche section to a large field of current research, with applications ranging from integrated circuits to medicine. Especially the field of research in the optical properties of nanostructures, known as nanooptics or plasmonics, has advanced significantly, and new facilities are constructed for further research in this still maturing section of nanosciences.
At the Kirchhoff Institute for Physics (KIP) at the University of Heidelberg, a new laboratory for plasmonic research has been constructed to investigate phase-transitioning nanoparticles using optical darkfield microscopy. In this thesis, first measurements using this new experimental setup will be presented, and comparisons to an existing setup at the Max Plank Institute for Intelligent Systems (MPI IS) in Stuttgart will be made. The purpose of this thesis was the calibration of the new microscope, and an in-depth test of all components of the setup to ensure proper function.
Parameters of the new setup such as the spectrum of the light source, effectively usable spectral range and long-term stability will be determined. In addition to this, two samples were manufactured, each of which contains nanodisks and nanorods of varying diameters or lengths, with resonances in the visible spectral range. The first sample is made of gold on an ITO/glass substrate, since gold is a well understood, easy to use and stable material for nanostructures. This sample will be used to verify the functionality of the new setup in both brightfield and darkfield mode, and will be brought to the MPI IS in Stuttgart to create measurements at a second microscope for the new setup to be compared to. The second sample features a multi-layer design with the ability to transition from a metallic, plasmonically active state into a non-metallic, inactive phase. It can thus be used to check the gas control system of the new installation including a custom designed gas cell.

2 Theoretical background

2.1 Plasmon polaritons

In condensed matter, there are two major types of excitations: phonons and plasmons. Phonons resemble collective oscillations of all lattice atoms in a crystal, whereas plasmons refer to collective oscillations of electrons. Phonons do not play a significant role in this thesis, the following will therefore focus on plasmons. A plasmon can be imagined as a longitudinally polarised wave of electrons, in which the charge carriers oscillate in a collective state. These collective oscillations of charged particles can now interact with the oscillating electric field of a photon and form a combined state: a so called plasmon polariton. These photon-plasmon states can be subdivided into three main categories:

1. Bulk plasmon polariton
2. Surface plasmon polariton
3. Particle plasmon polariton

In the following, the derivations of the mathematical description of these three types of plasmon polaritons will be explained.

2.1.1 Bulk Plasmon Polaritons

Bulk plasmon polaritons are propagating excitations in the bulk of a metal, ideally at an infinite distance from any surface. We will consider a homogeneous, isotropic metal. To derive their dispersion relation, we will begin with the Maxwell relations:

$$\mathrm{div}(\vec{D}) = \rho_{\mathrm{free}} \tag{1}$$

$$\mathrm{div}(\vec{B}) = 0 \tag{2}$$

$$\mathrm{rot}(\vec{E}) = -\frac{\partial \vec{B}}{\partial t} \tag{3}$$

$$\mathrm{rot}(\vec{H}) = \vec{j}_{\mathrm{free}} + \frac{\partial \vec{D}}{\partial t} \tag{4}$$

With $\vec{D} = \varepsilon_0 \varepsilon \vec{E}$ and $\vec{B} = \mu_0 \mu \vec{H}$. Since this thesis will only focus on non-magnetic media, and consider frequencies in the IR and higher, the approximation $\mu = 1$ works very well. Thus, μ will usually be considered to be equal to 1 in the following. We will also need the polarisation $\vec{P}$ of a medium with dielectric function ε given by

$$\vec{P} = \varepsilon_0 \chi_e \vec{E} = \varepsilon_0 (\varepsilon - 1) \vec{E} \tag{5}$$

This polarisation describes the dipole moment density in the medium which results from an external electric field. It can also be calculated from the electron density n, the electron charge e and the distance $\vec{r}$ by which the electrons in the medium have been shifted due to the external field:

$$\vec{P} = ne\vec{r} \tag{6}$$

With the Maxwell equations given above and under the assumption of the free current density $\vec{j}_{free} = 0$, the following can be derived:

$$\begin{aligned} \text{rot}(\text{rot}(\vec{E})) &= -\text{rot}\left(\frac{\partial \vec{B}}{\partial t}\right) \\ &= -\mu_0 \frac{\partial^2 \vec{D}}{\partial t^2} \\ &= -\frac{\varepsilon}{c^2}\frac{\partial^2 \vec{E}}{\partial t^2} \end{aligned} \tag{7}$$

With the well known identity

$$\Delta\vec{X} = \text{grad}(\text{div}(\vec{X})) - \text{rot}(\text{rot}(\vec{X})) \tag{8}$$

for the laplace operator Δ and any vector field $\vec{X}$, we can use the relation from 7 to calculate:

$$\begin{aligned} \Delta\vec{E} &= \text{grad}(\text{div}(\vec{E})) - \text{rot}(\text{rot}(\vec{E})) \\ &= \text{grad}(\text{div}(\vec{E})) + \frac{\varepsilon}{c^2}\frac{\partial^2 \vec{E}}{\partial t^2} \end{aligned} \tag{9}$$

If we now assume a periodic electric field of a propagating electromagnetic wave

$$\vec{E} = \vec{E_0} e^{i\vec{k}\vec{x} - i\omega t}$$

the result of 9 turns into:

$$k^2\vec{E} = \vec{k}\cdot(\vec{E}\cdot\vec{k}) + \frac{\varepsilon\omega^2}{c^2}\vec{E} \tag{10}$$

Now we will need the dielectric function of the metal to obtain the bulk plasmon polariton's dispersion relation. To derive the metal's dielectric function, we will use the Drude model, which models conduction electrons as a free electron gas. For such a free electron in an oscillating electric field, its movement is described by the following differential equation:

$$m_e\ddot{\vec{r}} + m_e\Gamma\dot{\vec{r}} = e\vec{E_0}e^{-i\omega t} \tag{11}$$

With electron position $\vec{r}$, effective electron mass m_e in the medium, electron charge e and dampening factor Γ. This differential equation can be solved by choosing the ansatz

$\vec{r} = \vec{r_0}e^{-i\omega t}$, the time derivatives of which can easily be calculated and put into equation 11:

$$\vec{r_0}\left(-m_e\omega^2 - im_e\omega\Gamma\right) = e\vec{E_0} \tag{12}$$

By multiplying both sides of the equation with the electron density n and the electron charge e, we can identify the polarisation $\vec{P}$ using equation 6, and replace it with equation 5:

$$\begin{aligned}\vec{r_0}ne\left(-m_e\omega^2 - im_e\omega\Gamma\right) &= ne^2\vec{E_0} \\ \Rightarrow \varepsilon &= 1 - \frac{\omega_p^2}{\omega^2 + i\omega\Gamma}\end{aligned} \tag{13}$$

Where we introduced the constant $\omega_p = \sqrt{\frac{ne^2}{\varepsilon_0 m_e}}$, the so-called plasma frequency, in the last step. This yields the dielectric function for a free electron gas, which we can use as a model for metals. As can clearly be seen, the dielectric function is complex and depends on the frequency of the oscillating field. To simplify the calculation further, we will now assume the dampening is very weak. This means Γ becomes very small and can be neglected:

$$\varepsilon = 1 - \frac{\omega_p^2}{\omega^2} \tag{14}$$

This very much simplified dispersion relation for light propagating through matter already offers some insights into the optical nature of metals. For example, a material's refractive index is given by $n = \sqrt{\varepsilon\mu}$. If we again assume μ to be equal to 1, this just leaves the square root of the dieletric function. As such, if the dielectric function is negative, the refractive index becomes purely imaginary, meaning that no light can penetrate the material, which thus becomes perfectly reflective. As can be seen from the dielectric function we just calculated, this is the case for all light with a frequency below the plasma frequency. This is why metals appear so reflective in the visible range: light in this range of frequencies is below the plasma frequency of most metals, and as a result they reflect most light in the visible range.

If we now assume a transverse electromagnetic wave, where $\vec{E}$ is orthogonal to the direction of propagation $\vec{k}$, the relation 10 is simplified:

$$k^2 = \frac{\varepsilon\omega^2}{c^2} \tag{15}$$

If we now replace ε with the dielectric function for the Drude model as derived in calculation 14, we obtain the dispersion relation for bulk plasmon polaritons:

$$\omega = \sqrt{\omega_p^2 + k^2c^2} \tag{16}$$

This dispersion relation is plotted in figure 1, it is clearly visible that bulk plasmon polaritons can not be excited below the plasma frequency, and how for larger frequencies

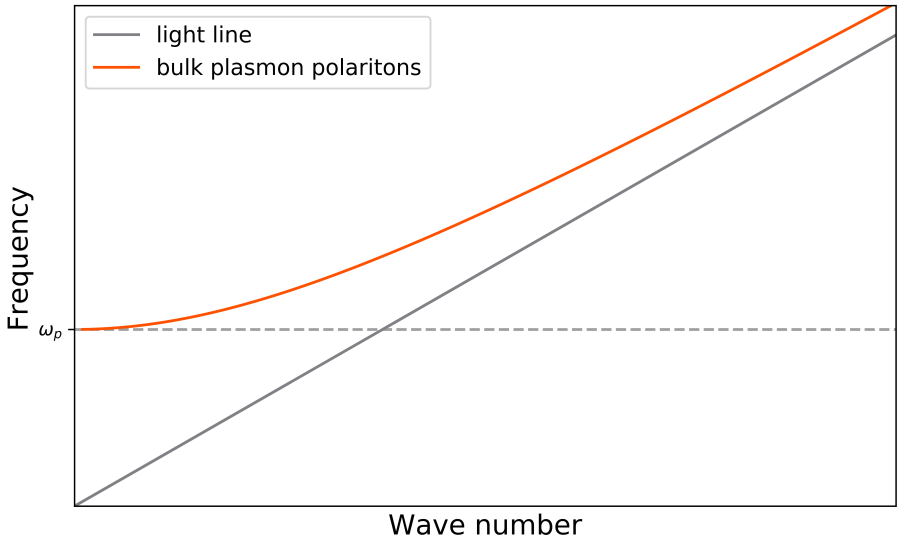

Figure 1: Dispersion relation for bulk plasmon polaritons as derived above. The grey line marks the light line, the dispersion relation for light in vacuum.

their behaviour more and more converges towards that of light in vacuum.

However, in reality, the dampening we have assumed to be zero in this calculation is not negligible, and bound electrons do also contribute to a metal's dielectric function. As such, especially for shorter wavelengths the real dielectric function of gold does vary significantly from the Drude model we have used here. To demonstrate these differences in the visible spectral range, the dielectric function of gold as derived from the Drude model in equation 13 is plotted in figure 2, alongside experimental results for the dielectric function of evaporated gold taken from R. L. Olmon et al., Phys. Rev. B (2012). The differences between reality and the model of a free electron gas are clearly visible. It also needs to be noted that the dielectric function also depends on the crystal structure, impurities and the manufacturing process of a specific structure. The dielectric functions of metals like gold vary depending on multiple parameters, and are not always the same.

The contribution of bound electrons can be calculated similarly to the contribution of the free electron gas, however there is an additional term in the differential equation describing their motion due to the restoring force acting upon the bound electrons:

$$m_e\ddot{\vec{r}} + m_e\gamma\dot{\vec{r}} + m_e\omega_0^2\vec{r} = e\vec{E_0}e^{-i\omega t} \tag{17}$$

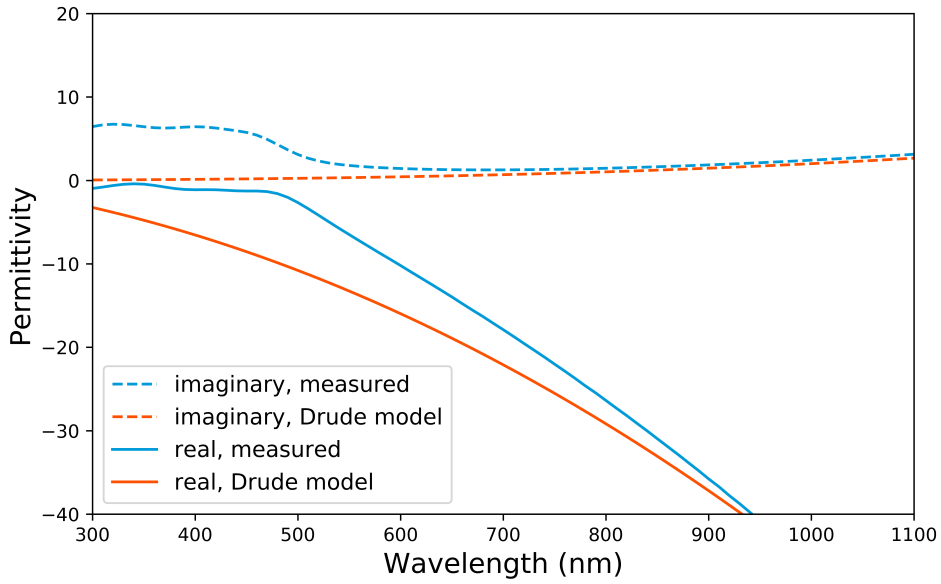

Figure 2: Comparison of experimental results for the dielectric function of evaporated gold (data from R. L. Olmon et al., Phys. Rev. B (2012)) with a fit of the Drude model as derived in equation 13.

Here we have assumed the restoring force to be harmonic. If we proceed as we did for the free electron gas, the additional contribution of the bound electrons to the dielectric function can be calculated. The full dielectric function in this model is then given by the sum of both contributions:

$$\varepsilon_{full} = \varepsilon_{Drude} + \varepsilon_{bound} = 2 - \omega_p^2 \left(\frac{1}{\omega^2 + i\omega\Gamma} - \frac{1}{(\omega_0^2 - \omega^2) - i\omega\gamma} \right) \tag{18}$$

2.1.2 Surface plasmon polaritons

On the surface of metals, or more precisely on metal-dielectric interfaces, electromagnetic excitations which propagate along the surface are possible. These surface plasmon polaritons (SPPs) are localized on the interface, and decay exponentially both into the metal as well as the dielectric. To deduce the characteristics of such a plasmon polariton, we will now consider a half space with a metal-dielectric interface. The interface itself shall be the x-y-plane, with the volume with $z > 0$ being a dielectric medium with a constant dielectric function ε_d, and the volume with $z < 0$ being metal, with a complex and frequency dependent dielectric function $\varepsilon(\omega)$. A surface plasmon polariton shall propagate along the interface in the x-direction. Since we consider an isotropic space in the x- and y-direction, all following calculations will be true for any propagation vector in the x-y-plane. Since our SPP propagates along the x-axis, and shall decay in both z-directions away from the interface, its wave vector looks like this:

$$\text{in dielectric}: \ \vec{k_d} = \begin{pmatrix} k_1 \\ 0 \\ ik_3^d \end{pmatrix} \qquad \text{in metal}: \ \vec{k_m} = \begin{pmatrix} k_1 \\ 0 \\ -ik_3^m \end{pmatrix} \tag{19}$$

Both vectors share the same value for k_1, since it is a single SPP with a fixed propagation. The values ik_3^m and ik_3^d are complex, since the SPP decays in both directions orthogonal to the interface.

We will now consider the Maxwell equations for our SPP in both the metal and the dielectric. We will first look at a transverse magnetic (TM) wave, where the magnetic field is perpendicular to the direction of propagation. The magnetic and electric fields of our

SPP in both media are then defined by:

$$\text{in dielectric}: \; H_d(\vec{x},t) = \begin{pmatrix} 0 \\ A \\ 0 \end{pmatrix} e^{ik_1 x_1 - k_3^d x_3 - i\omega t} \qquad E_d(\vec{x},t) = -A\frac{c}{i\omega\varepsilon_0\varepsilon_d} \begin{pmatrix} k_3^d \\ 0 \\ ik_1 \end{pmatrix} e^{ik_1 x_1 - k_3^d x_3 - i\omega t}$$

$$\text{in metal}: \; H_m(\vec{x},t) = \begin{pmatrix} 0 \\ B \\ 0 \end{pmatrix} e^{ik_1 x_1 + k_3^m x_3 - i\omega t} \qquad E_m(\vec{x},t) = -B\frac{c}{i\omega\varepsilon_0\varepsilon(\omega)} \begin{pmatrix} -k_3^m \\ 0 \\ ik_1 \end{pmatrix} e^{ik_1 x_1 + k_3^m x_3 - i\omega t} \tag{20}$$

Where A and B are unspecified constants and the Maxwell equation 4 has been used to deduce the amplitude of the electric field from the amplitude of the magnetic field, assuming there are no external stimuli.
As can easily be derived from the Maxwell equations, at an interface between two materials, the electric and magnetic field components parallel to the surface have to be continuous at the interface. This yields the following results:

1. continuity of the magnetic field at $x_3 = 0$:

$$A \stackrel{!}{=} B$$

2. continuity of the x-component of the electric field at $x_3 = 0$:

$$A\frac{k_3^d}{\varepsilon_d} \stackrel{!}{=} -B\frac{k_3^m}{\varepsilon(\omega)}$$

These conditions combined give the following important relation:

$$\frac{k_3^d}{k_3^m} = -\frac{\varepsilon_d}{\varepsilon(\omega)} \tag{21}$$

We know that both k_3^d and k_3^m need to be real as well as positive, otherwise our SPP would not decay in both directions perpendicular to the interface. We also have assumed ε_d to be positive. Thus, in order for this relation to be fulfilled, $\varepsilon(\omega)$ has to be negative. If we now remember the dielectric function for metals we derived from the Drude model, equation 14, we can see that this is only the case for frequencies below the plasma frequency. As such, SPPs behave exactly opposite to bulk plasmon polaritons: In the frequency region below ω_p only SPPs are possible, but no bulk plasmon polaritons. For frequencies above ω_p SPPs can not exist, but bulk plasmon polaritons can be excited. To get the dispersion relation for SPPs, we will use the following relations which can easily be derived from the

wave vectors 19 of the SPP in the different media, as well as relation 15. If we compare these, we can obtain the following result:

$$\begin{aligned} k_d^2 &= \frac{\varepsilon_d \omega^2}{c^2} = k_1^2 - (k_3^d)^2 \\ k_m^2 &= \frac{\varepsilon(\omega)\omega^2}{c^2} = k_1^2 - (k_3^m)^2 \end{aligned} \tag{22}$$

These can easily be solved for the k_3 components. If we then substitute these components in equation 21, we can finally derive the dispersion relation for surface plasmon polaritons:

$$\omega = \sqrt{\frac{\varepsilon_d + \varepsilon(\omega)}{\varepsilon_d \varepsilon(\omega)}} k_1 c \tag{23}$$

We have already seen that SPPs can only be excited if $\varepsilon(\omega)$ is negative, assuming ε_d and k_1 are both real and positive. Since ω in the dispersion relation above also needs to be real and positive, this means that in addition to being negative, the magnitude of $\varepsilon(\omega)$ has to be greater than the magnitude of ε_d for SPPs to exist.

Transverse magnetic surface plasmon polaritons can be derived from the Maxwell equations.
For transverse electric (TE) waves, the method of derivation shown above yields the following result (see [1]):

$$k_3^d = -k_3^m \tag{24}$$

This result however contradicts one of the assumptions we made at the beginning of this chapter: we assumed an excitation which is localized on the interface, and as such decays exponentially into both the metal and the dielectric. This will only be the case if both k_3^d and k_3^m are real and positive, and the relation above contradicts this requirement, since both k_3^d and k_3^m are either zero, or one of them is negative, which would indicate exponential increase in the amplitude of the electric field with increasing distance from the interface, which is physically impossible. Since only TM SPPs can exist, we will from now on refer to them simply as SPPs.

The dispersion relation for SPPs (equation 23) can be seen in figure 3. It is well visible how it converges towards a constant frequency, ω_{SP}, for large wave vectors. To calculate this frequency, we just need to find the frequency at which the prefactor in equation 23

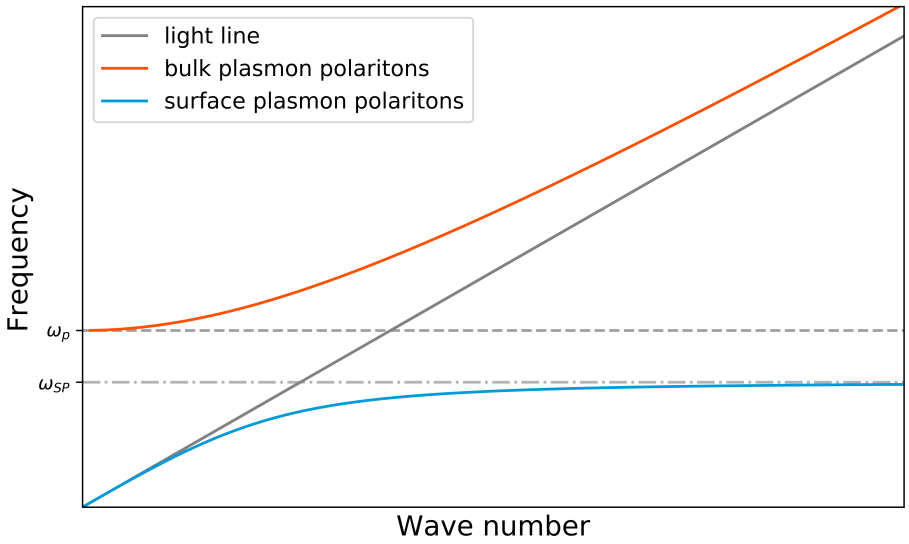

Figure 3: Dispersion relation for both bulk plasmon polaritons and surface plasmon polaritons as derived above. The grey line marks the light line, the dispersion relation for light in vacuum.

reaches zero. We will insert the Drude model dielectric function for $\varepsilon(\omega)$:

$$\sqrt{\frac{\varepsilon_d + \left(1 - \frac{\omega_p^2}{\omega_{SP}^2}\right)}{\varepsilon_d \cdot \left(1 - \frac{\omega_p^2}{\omega_{SP}^2}\right)}} \stackrel{!}{=} 0 \tag{25}$$
$$\Rightarrow \omega_{SP} = \omega_p \sqrt{\frac{1}{1 + \varepsilon_d}}$$

Another effect of the dispersion relation of SPPs can also easily be seen in figure 3: An SPP at a certain frequency ω always has a different wave vector compared to light in vacuum. As such, at the same energy, an SPP has a different impulse than a photon. This means that SPPs can not be directly excited by shining ordinary light on a metal surface, and makes special setups necessary to research them.

2.1.3 Particle plasmon polaritons

On small metallic particles, electromagnetic waves can cause collective oscillations of all electrons in the particle. These plasmon polaritons, which are localized on the nanoparticle, are called particle plasmon polaritons (PPPs) or localized surface plasmon polaritons (LSPPs), and their behaviour is highly dependent on the material of the particle, the surrounding medium, as well as the size and shape of the particle. These usually non-trivial dependencies make the mathematical description of these resonances rather difficult, and for most shapes time-consuming numerical simulations are the only possible option. For spheres and other particles with rotational symmetry however, an exact analytical solution does exist. The theory for the scattering of homogeneous plane waves on spheres of any size as derived by Gustav Mie [2] breaks all electric and magnetic fields up into infinite series of spherical functions, each representing an excitable multi-pole mode of increasingly higher order. For this approach, the so-called Mie-scattering, a transformation into spherical coordinates is necessary.

A vector (x, y, z) is now defined by a distance r from the origin as well as the polar angle θ and the azimuth angle Φ which are defined as follows:

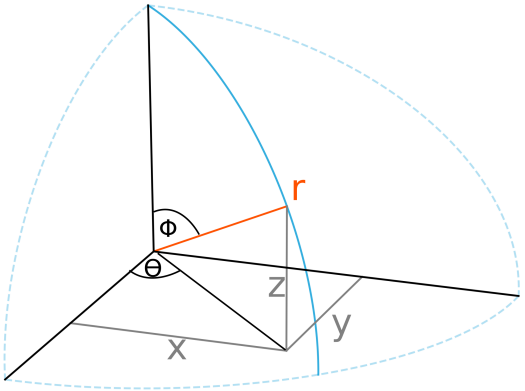

$$\begin{aligned} r &= \sqrt{x^2 + y^2 + z^2} \\ \theta &= \arccos\left(\frac{z}{x}\right) \\ \Phi &= \arctan\left(\frac{y}{x}\right) \end{aligned} \tag{26}$$

Furthermore, we will use the following forms of electric and magnetic fields:

$$\begin{aligned} E_r &= \mathcal{E}_r \cdot e^{i\omega t} \\ H_r &= \mathcal{H}_r \cdot e^{i\omega t} \end{aligned} \tag{27}$$

The same shall be done for all vector components of $\vec{E}$ and $\vec{H}$. Here, $\mathcal{E}_r$ and $\mathcal{H}_r$ are only dependent on the coordinates, but not on time. Finally, we will introduce the variable $\mathcal{M}_r$ given by

$$-\frac{i \cdot c}{n} \cdot \mu_0 \mathcal{H}_r = \mathcal{M}_r \tag{28}$$

(same for all other vector components of $\vec{\mathcal{H}}$)
In these coordinates, a propagating, oscillating electromagnetic field with linear polarisation can be expanded as the following infinite sums of spherical functions:

$$\begin{aligned} \mathcal{E}_r &= A \cdot \sum_{n=1}^{\infty} (2n+1) i^{n-1} \frac{I_n}{(kr)^2} P_n \\ \mathcal{E}_\theta &= A \cdot \sum_{n=1}^{\infty} \left[\frac{2n+1}{n(n+1)} i^{n-1} \frac{I_n'}{kr} \frac{\partial P_n}{\partial \theta} \qquad + \frac{2n+1}{n(n+1)} i^n \frac{I_n}{kr \cdot \sin(\theta)} \frac{\partial \tilde{P}_n}{\partial \Phi} \right] \\ \mathcal{E}_\Phi &= 0 \end{aligned} \tag{29}$$

Here, A represents a constant amplitude, I_n are functions of the radius r and the functions P_n and $\tilde{P}_n$ are spherical functions of the two vectors θ and Φ. Even though we are considering a propagating electromagnetic wave, due to our definition of $\vec{\mathcal{E}}$ no oscillation term depending on time appears here. This linearly polarised electromagnetic wave represents the incoming wave.

We are interested in the electromagnetic properties of a metallic sphere with the radius a. This sphere shall be at the centre of the coordinate system. To derive expressions for the electric field inside and outside the sphere when light of a known wavelength is

incident on it, we need to consider the boudary conditions at the surface of the sphere:

$$\begin{aligned} \mathcal{E}_{\theta,e} &\stackrel{!}{=} \mathcal{E}_{\theta,i}, \qquad \mathcal{E}_{\Phi,e} \stackrel{!}{=} \mathcal{E}_{\Phi,i} \\ n_d \cdot \mathcal{M}_{\theta,e} &\stackrel{!}{=} n(\omega) \cdot \mathcal{M}_{\theta,i}, \qquad n_d \cdot \mathcal{M}_{\Phi,e} \stackrel{!}{=} n(\omega) \cdot \mathcal{M}_{\Phi,i} \end{aligned} \tag{30}$$

The process of deriving the internal and scattered fields of the sphere is a very labour intensive calculation, and will thus not be shown here. Please refer to [2] or [3] for the full process of derivation.

The expressions for the internal field are again represented by infinite series of spherical functions:

$$\begin{aligned} \mathcal{E}_{r,i} &= A \cdot \sum_{n=1}^{\infty} i \cdot b_n \frac{I_n}{(kr)^2} P_n \\ \mathcal{E}_{\theta,i} &= A \cdot \sum_{n=1}^{\infty} \left[\frac{i \cdot b_n}{n(n+1)} \cdot \frac{I_n'}{kr} \frac{\partial P_n}{\partial \theta} + \frac{q_v}{n(n+1)} \cdot \frac{I_n}{kr \cdot \sin(kr)} \cdot \frac{\partial \tilde{P}_n}{\partial \Phi} \right] \\ \mathcal{E}_{\Phi,i} &= A \cdot \sum_{n=1}^{\infty} \left[\frac{i \cdot b_n}{n(n+1)} \cdot \frac{I_n'}{kr \cdot \sin(kr)} \frac{\partial P_n}{\partial \Phi} - \frac{q_v}{n(n+1)} \cdot \frac{I_n}{kr} \cdot \frac{\partial \tilde{P}_n}{\partial \theta} \right] \end{aligned} \tag{31}$$

Where the constants b_n represent the effect of electric multipole modes of the sphere and q_n the effect of magnetic multipole modes. For the scattered field, very similar expressions can be found. It should be noted that these only represent the scattered fields, even though the external field is the sum of the incoming and scattered fields:

$$\begin{aligned} \mathcal{E}_{r,s} &= A \cdot \sum_{n=1}^{\infty} i \cdot a_n \frac{K_n}{(kr)^2} P_n \\ \mathcal{E}_{\theta,s} &= A \cdot \sum_{n=1}^{\infty} \left[\frac{i \cdot a_n}{n(n+1)} \cdot \frac{K_n'}{kr} \frac{\partial P_n}{\partial \theta} + \frac{p_n}{n(n+1)} \frac{K_n}{kr \cdot \sin(kr)} \cdot \frac{\partial \tilde{P}_n}{\partial \Phi} \right] \\ \mathcal{E}_{\Phi,s} &= A \cdot \sum_{n=1}^{\infty} \left[\frac{i \cdot a_n}{n(n+1)} \cdot \frac{K_n'}{kr \cdot \sin(kr)} \frac{\partial P_n}{\partial \Phi} - \frac{p_n}{n(n+1)} \frac{K_n}{kr} \cdot \frac{\partial \tilde{P}_n}{\partial \theta} \right] \end{aligned} \tag{32}$$

Similarly to the internal fields, the constants a_n and p_n correspond to the effects of the electric and magnetic multipoles, respectively.

These equations offer an analytical description of the internal and scattered fields of a metallic sphere of arbitrary size, from sub-wavelength to macroscopic, on which a planar wave of arbitrary wavelength is incident. It is therefore a very powerful result and has applications from meteorology to astrophysics **??**. For our purpose however, these equations are rather complicated, and since we will only concern ourselves with particles much smaller than the wavelength of light, we can make a few approximations to greatly simplify these results:

1. Only the first electric mode is relevant
   As Mie derived, the constants a_n, b_n, p_n and q_n become very small for small particles relative to the wavelength of the incident light with increasing n. Since this is even more severe for the magnetic modes, we will only have to consider the values of a_1 and b_1, and can consider all other constants to be zero.

2. Quasistatic electric field
   Since the wavelength of the light is much bigger than our particle, it effectively has the same phase across the entire particle. This means we can assume a quasistatic incoming field rather then an oscillating one, which means we can assume k to be zero.

By assuming these approximations, Mie's result turns into Rayleigh-scattering. First, we will put in the value Mie derived for b_1 (see [2]) into the expressions for the internal fields, and assume all other constants to be negligible:

$$\begin{aligned}
\mathcal{E}_{r,i} &= A \cdot \left(\frac{3\varepsilon_d}{\varepsilon(\omega) + 2\varepsilon_d}\right) \cdot \left(\frac{\sin(kr)}{kr} - \cos(kr)\right) \frac{1}{(kr)^2} \cdot \cos(\theta) \\
\mathcal{E}_{\theta,i} &= A \cdot \left(\frac{3\varepsilon_d}{\varepsilon(\omega) + 2\varepsilon_d}\right) \cdot \left(\sin(kr) + \frac{\cos(kr)}{kr} - \frac{\sin(kr)}{(kr)^2}\right) \frac{1}{kr} \cdot (-\sin(\theta)) \\
\mathcal{E}_{\Phi,i} &= 0
\end{aligned} \tag{33}$$

Since these functions are for now not defined at k = 0, we will have to do an analytical expansion by substituting the trigonometric functions by their Taylor-expansion to the second order for very small k. We will then see that k cancels out, and by assuming k = 0 the approximation for small k will become exact. By then rearranging the terms, we can arrive at the final result for the internal electric field:

$$\begin{aligned}
\mathcal{E}_{r,i} &= \left(\frac{3\varepsilon_d}{\varepsilon(\omega) + 2\varepsilon_d}\right) \cdot A \cdot \cos(\theta) \\
\mathcal{E}_{\theta,i} &= \left(\frac{3\varepsilon_d}{\varepsilon(\omega) + 2\varepsilon_d}\right) \cdot A \cdot (-\sin(\theta)) \\
\mathcal{E}_{\Phi} &= 0 \\
\Rightarrow \vec{\mathcal{E}}_{\text{internal}} &= \left(\frac{3\varepsilon_d}{\varepsilon(\omega) + 2\varepsilon_d}\right) \cdot A \cdot \left(\cos(\theta) \cdot \vec{e}_r - \sin(\theta) \cdot \vec{e}_\theta\right) \\
&= \left(\frac{3\varepsilon_d}{\varepsilon(\omega) + 2\varepsilon_d}\right) \cdot \vec{\mathcal{E}}_{\text{incident}}
\end{aligned} \tag{34}$$

Where we have utilized that $\left(\cos(\theta) \cdot \vec{e}_r - \sin(\theta) \cdot \vec{e}_\theta\right) = \vec{e}_r$ by the definition of spherical coordinates and that $A \cdot \vec{e}_r = \vec{\mathcal{E}}_{\text{incident}}$ in our assumption of a quasi-static electric field along the x-axis.

Before further analysing this result, we will first derive a simplified version of the external field as well. As before, we will neglect all constants but a_1 in the expressions 32, and

then proceed to set k to zero:

$$\mathcal{E}_{r,s} = 2A \cdot \left(a^3 k^3 \frac{\varepsilon(\omega) - \varepsilon_d}{\varepsilon(\omega) + 2\varepsilon_d} \right) \cdot \frac{1}{(kr)^3} e^{-ikr} \left[1 + ikr \right] \cdot \cos(\theta) \tag{35}$$

$$\mathcal{E}_{\theta,s} = \quad A \cdot \left(a^3 k^3 \frac{\varepsilon(\omega) - \varepsilon_d}{\varepsilon(\omega) + 2\varepsilon_d} \right) \cdot \frac{1}{(kr)^3} e^{-ikr} \left[1 + ikr - (kr)^2 \right] \cdot \sin(\theta) \tag{36}$$

$$\mathcal{E}_{\Phi,s} = \quad 0 \tag{37}$$

These functions, after very little rearrangement, are already defined for k = 0, so no analytical expansion is required here. This then yields the following expression for the external field:

$$\begin{aligned} \mathcal{E}_{r,s} &= 2A \cdot \left(\frac{\varepsilon(\omega) - \varepsilon_d}{\varepsilon(\omega) + 2\varepsilon_d} \right) \cdot \frac{a^3}{r^3} \cos(\theta) \\ \mathcal{E}_{\theta,s} &= \quad A \cdot \left(\frac{\varepsilon(\omega) - \varepsilon_d}{\varepsilon(\omega) + 2\varepsilon_d} \right) \cdot \frac{a^3}{r^3} \sin(\theta) \\ \mathcal{E}_{\Phi,s} &= \quad 0 \\ \Rightarrow \vec{\mathcal{E}}_{\text{external}} &= \vec{\mathcal{E}}_{\text{incident}} + A \cdot \left(\frac{\varepsilon(\omega) - \varepsilon_d}{\varepsilon(\omega) + 2\varepsilon_d} \right) \cdot \frac{a^3}{r^3} \cdot \left(2\cos(\theta)\vec{e}_r + \sin(\theta)\vec{e}_\theta \right) \end{aligned} \tag{38}$$

Where we have introduced the unit vectors $\vec{e}_r$ and $\vec{e}_\theta$ in the corresponding directions.
These simplified expressions for the internal and scattered fields, derived as an approximation for a very small sphere in a quasi-static electric field, are much easier to interpret. From expression 34 for example we can see, that the electric field inside the nanosphere is, at least in this approximation, independent of the location. As such, the electric field inside the particle is homogeneous. On the outside on the other hand, as can be seen from 38, the electric field proportional to r^{-3}. In fact, the external electric field does represent the field caused by a dipole. That a nanosphere in an external electric field behaves like a dipole is a very important conclusion from these derivations.
We can also see that the internal as well as the external fields will both diverge if the condition

$$\varepsilon(\omega) = -2\varepsilon_d \tag{39}$$

is met. This results in resonant excitation of the plasmon polariton of the particle. Due to the direct dependency of this resonance condition on the surrounding material, nanoparticles can be used for sensing by monitoring their resonance frequencies.

Mie's results also allow the calculation of the cross-sections of absorption and scattering for metallic spheres. With the simplifying assumptions for nanospheres and optical wavelengths, the following dependencies of the cross-sections on the particle diameter a

can be obtained (see [5], [6]):

$$\begin{aligned} \sigma_{\text{scattering}} &= \frac{8\pi}{3} k^4 a^6 \left| \frac{\varepsilon(\omega) - \varepsilon_d}{\varepsilon(\omega) + 2\varepsilon_d} \right| \propto a^6 \\ \sigma_{\text{absorption}} &= 4\pi k a^3 \text{Im} \left[\frac{\varepsilon(\omega) - \varepsilon_d}{\varepsilon(\omega) + 2\varepsilon_d} \right] \propto a^3 \end{aligned} \tag{40}$$

As such, for very small particles the absorption dominates the interaction with light, whereas for larger particles the scattering of light takes over.

In 1912, Richard Gans published a small variation on Mie's theory for scattering on spheres, where Gans generalized Mie's theory for any spheroid, considering particles much smaller than the wavelength of the incident light [4]. As has been alluded to at the beginning of this chapter, the mathematical description of plasmonic resonances in small particles is rather difficult, and generally not analytically possible. Since in this thesis measurements on nanorods and nanodisks where done, but not however on spheres, Mie's theory is not yet applicable as a well-suited theoretical model for the conducted experiments. Since however for both the nanorods, which are of rectangular shape, and the nanodisks no analytical description exists, the understanding of the behaviour of spheroids (elongated for the rods and squashed for the disks) will have to serve as the best possible approximation, and will already offer valuable insights into the general behaviour of our structures.

Spheroids, due to the lower symmetry compared to perfect spheres, display two distinct excitation modes instead of one. Since length and width of spheroids differ, the excitations along the axis of rotational symmetry have a different resonance than the modes perpendicular to it. Since an electric field component in the direction of the mode is required to excite it, polarised light can be used to excite a specific mode if the direction of polarisation is chosen correctly.

To derive the mathematical description, we will again assume a quasi-static electric field due to the small particle size compared to the wavelength of light. We shall now assume a spheroid particle at the origin of a coordinate system (x,y,z), with the particles axis of rotational symmetry being aligned with the x-axis of the coordinate system. Gans has derived the following expressions for the electric field components inside the particle:

$$\begin{aligned} E_x &= \frac{1}{1 + (\frac{\varepsilon(\omega)}{\varepsilon_d} - 1) \cdot L} \cdot E_x^0 \\ E_y &= \frac{1}{1 + (\frac{\varepsilon(\omega)}{\varepsilon_d} - 1) \cdot L'} \cdot E_y^0 \\ E_z &= \frac{1}{1 + (\frac{\varepsilon(\omega)}{\varepsilon_d} - 1) \cdot L'} \cdot E_z^0 \end{aligned} \tag{41}$$

Where, as before, $\varepsilon(\omega)$ refers to the dielectric function of the particle and ε_d to the dielectric function of the medium the particle is embedded in. Here, the value of L depends on the ratio of long and short axis of the spheroid particle, and is defined by either

$$L = \frac{1 - e^2}{e^2} \cdot \left(\frac{1}{2e} \cdot \ln\left(\frac{1 + e}{1 - e} \right) - 1 \right) \tag{42}$$

in case of an elongated spheroid or by

$$L = \frac{1}{e^2} \cdot \left(1 - \frac{\sqrt{1 - e^2}}{e} \arcsin(e) \right) \tag{43}$$

for squashed spheroids. The ellipticity e is defined by

$$e^2 = 1 - \left(\frac{b}{a} \right)^2 \tag{44}$$

where a is the length of the longer axis of the particle and b the shorter axis. The values L' are given by

$$L' = \frac{1 - L}{2}$$

As such, a perfect sphere would have an ellipticity of $e = 0$, which means that $L = L' = \frac{1}{3}$. If we use these values in the equations 41, we can easily see that for a sphere, the internal electric field in Gans-theory is exactly what Mie derived for the internal field of very small spheres, as seen in 34. From the equations 41 we can already derive the resonance wavelength of the plasmon polariton excitation along a given axis: at the resonance wavelength, the internal electric field will be maximal. And from the equations above we can see that the internal electric field of a small spheroid particle will diverge if the following condition is met:

$$1 + \left(\frac{\varepsilon(\omega)}{\varepsilon_d} - 1 \right) \cdot L \stackrel{!}{=} 0 \tag{45}$$

for the resonance along the axis of rotational symmetry, or

$$1 + \left(\frac{\varepsilon(\omega)}{\varepsilon_d} - 1 \right) \cdot L' \stackrel{!}{=} 0 \tag{46}$$

for resonances orthogonal to the axis of rotational symmetry. If we now substitute the equation 13for $\varepsilon(\lambda)$ in the conditions for resonance, we can obtain the following equations for the wavelength of light in vacuum at which the particle resonates:

$$\begin{aligned} \lambda_{res}^2 &= \lambda_p^2 \cdot \left(1 - \varepsilon_d \cdot \left(1 - \frac{1}{L} \right) \right) \\ \lambda_{res}'^2 &= \lambda_p^2 \cdot \left(1 - \varepsilon_d \cdot \left(1 - \frac{1}{L'} \right) \right) \end{aligned} \tag{47}$$

Where λ_{res} refers to the resonance along the axis of rotation and λ'_{res} to resonances perpendicular to it.

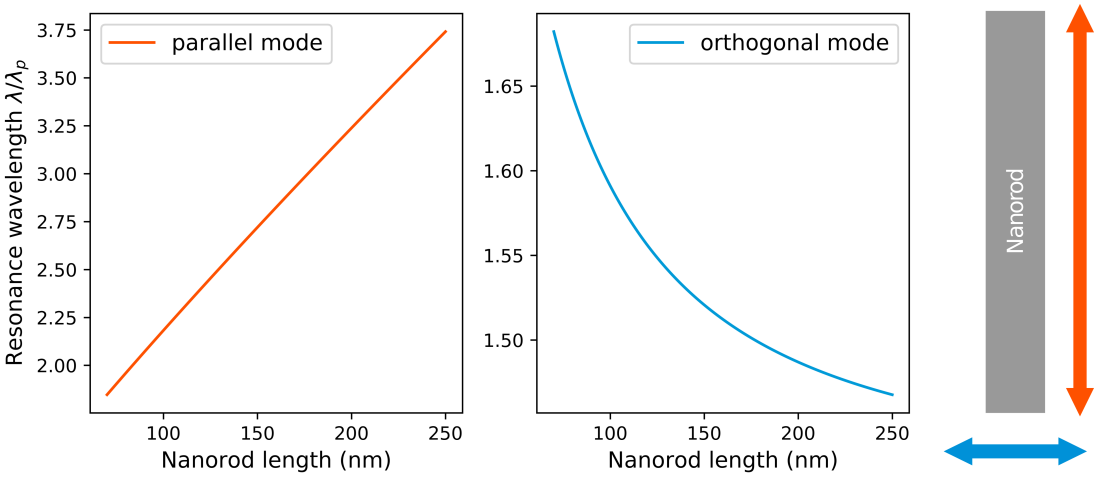

Figure 4: Resonance wavelengths for parallel (left) and orthogonal (right) mode as calculated with equations 47 for spheroid nanoantennas with a constant width of 60nm and varying lengths.

To get an impression of these results for the resonance wavelength, they have been plotted in 4 for spheroid nanoantenna of different lengths between 70nm and 250nm and a constant width of 60nm. It is well visible that according to Gans-theory, with increasing length the resonance wavelength of the mode parallel to the axis of rotational symmetry also increases in a mostly linear fashion, whereas the resonance frequency of the perpendicular mode decreases, even though the particle width remains unchanged.

2.2 Phase transitioning materials

Certain materials like palladium, yttrium or magnesium, can incorporate hydrogen atoms into their crystal structure. In this process called hydrogenation, a metal hydride is formed. Many of these hydrides are non-metallic, which allows the materials to be actively switched from a metallic form to a dielectric form. Since metals and dielectrics have significantly different optical properties, these phase-transitioning materials have a large potential for active optics.

2.2.1 Magnesium Nanoparticles

As was previously explained, the existence of free electrons is crucial for the excitation of any kind of plasmon polariton. Free electrons only exist in metals, and as such phase transitions from a metal to a dielectric can be used to actively switch the plasmonic prop-

erties of the material. This can be used to design nanoparticles which can be switched off even after manufacture.

The application of reversibly switchable magnesium nanoparticles has been introduced by Florian Sterl et al [7]. Magnesium can store a very large amount of hydrogen (up to 7,6% by weight, [7]), and its hydrogenation can be reversed, which makes it an ideal metal for phase transitioning nanoparticles. However, it has no catalytic properties, and can thus not split hydrogen gas into its atomic form. This is however needed for the hydrogenation to happen. This is why the magnesium structures need to be covered with a very thin layer of palladium. The palladium layer acts as a catalyst, splitting up hydrogen gas into hydrogen atoms, and aiding the catalytic oxidation of the stored hydrogen to revert the hydrogenation process.

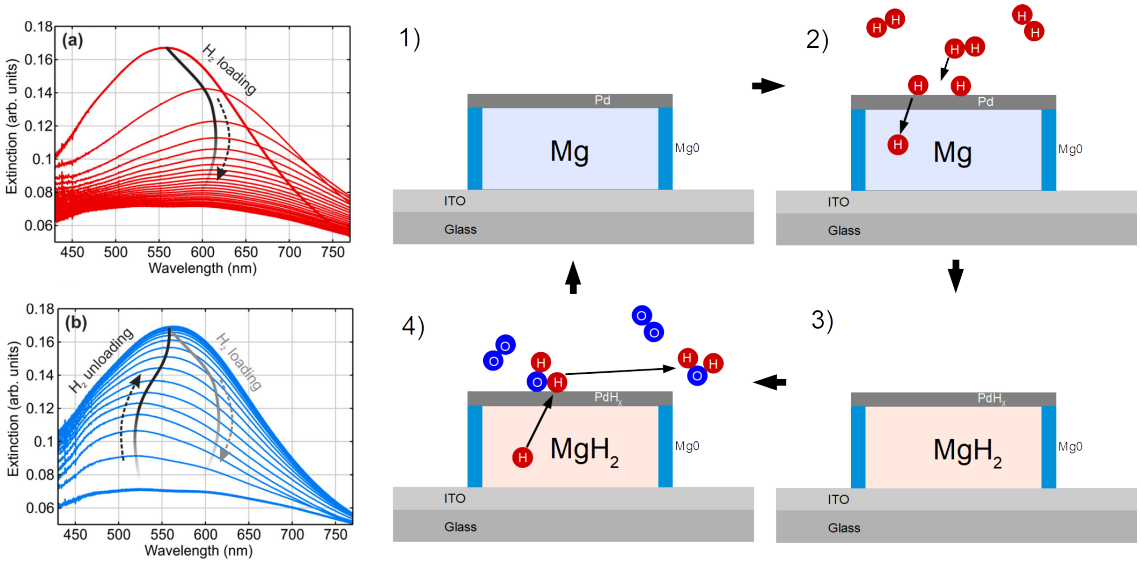

Figure 5: On the left: changes in the extinction of magnesium nanodisks during hydrogen loading (top, red) and unloading (bottom, blue), from [7]. On the right: schematic visualization of hydrogen loading (2) and hydrogen unloading (4). The cycle can be repeated numerous times.

To hydrogenate these structures, they simply have to be exposed to a hydrogen atmosphere for a few minutes. The structures will by themselves absorb the hydrogen and transition into the non-metallic hydride phase. To revert the hydrogenation, they are exposed to oxygen, which at the palladium surface will react with the hydrogen to form water. In the paper by Florian Sterl et al, for hydrogenation a concentration of 4% H_2 in N_2 was used, and the hydrogen loading took less than 10 minutes for nanodisks of a diameter of 220nm. Dehydrogenation was done using 5% O_2 in N_2 and took less than

30 minutes.

During hydrogenation the structures increase in their volume by roughly 30%, and then retract again if exposed to oxygen to reverse the process. This causes the material to become porous and brittle, and causes fatigue. Another cause of damage to the magnesium nanoparticles are water and carbon dioxide in the ambient air, which is why proper care needs to be taken to minimize the time the structures spend in air.

3 Experimental methods

3.1 Dark field microscopy

The main difference between a dark field microscope and the more commonly used bright field version, is the so-called 'dark field condenser'. This optical element is used to direct the light of the light source onto the sample in a very specific way: Usually, in a bright

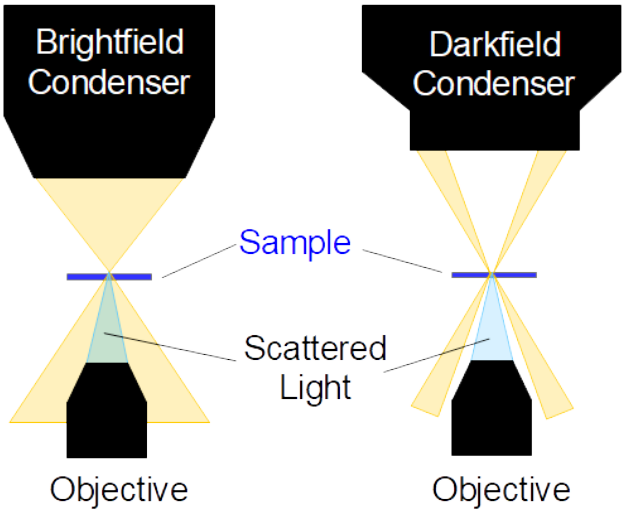

Figure 6: Schematic comparison of how the scattered light is directed onto the sample in bright field (left) and dark field (right). The transmitted light reaches the objective in the bright field case, but not in the dark field setup.

field setup, the light is directed onto the sample as a solid cone with a certain opening angle, a two-dimensional schematic of which can be seen on the left in figure 6. Since in transmission geometry, the objectives are directly in line with the condenser, here some of the incident light which is transmitted by the sample makes its way into the objective. This creates a very bright background for the generated image, with the structures on the sample themselves dark against it. If the structures are very small and very disperse, they may not even be visible at all. In a dark field setup, the dark field condenser is used to direct the light at the sample not in a solid cone, but a hollow one. This, as can be more clearly seen in figure 6 on the right, means that the transmitted incident light does no longer reach the objective, but misses it. As such, the only light caught by the objective is the light scattered by the sample. Even small and disperse structures appear as bright spots against the dark background and are clearly visible. This makes dark field

microscopy a very useful tool in the research of plasmonic resonances, and even allows the measurement of the spectrum of a single particle.

3.2 Transmission Setup

Most measurements were taken using a newly installed microscopy and spectroscopy setup. The setup is based around a Nikon Eclipse Ti-U inverted microscope, which allows for brightfield as well as darkfield microscopy in transmission geometry. For increased mid-term stability, the original Nikon light source has been replaced by a laser driven light source (LDLS), model EQ99X by Energetiq, which provides a continuous spectrum across the entire visible range. A motorized stage by Märzhäuser has been installed, and allows for largely automated measurements in combination with the custom software. To analyse the spectra of samples, a spectrometer (Acton SpectraPro SP-2500) with a CCD sensor (PIXIS 256) by Princeton Instruments is attached to the left port of the microscope. The spectrometer covers the entire visible range, and the CCD sensor is Peltier-cooled to decrease thermal noise. A camera along the optical path of the microscope can be used for real time imaging. The microscope, light source and spectrometer are contained within a protective PVC shroud, to prevent dust and external light from influencing measurements. To research phase-transitioning nanostructures and materials, a gas system is available, which can control the flow of multiple attached gasses with a precision of 1% of the desired flow. Attached are gases like nitrogen, hydrogen, oxygen, carbon dioxide as well as carbon monoxide and argon. A gas cell for controlling the atmosphere around a sample while simultaneously doing measurements on it in the microscope has been designed. A custom computer program can be used to control the stage, spectrometer, real-time camera and gas system, and allows for powerful data processing.

In figure 7, pictures of the setup can be seen. Important components are marked by green frames: (1) marks the microscope itself. On the left of the microscope, the spectrometer is located (2). On the right of the microscope, housed in a small aluminium housing which doubles as a heat sink, is the laser driven light source. The laser which drives the LDLS is located outside the enclosure of the microscope, since its cooling fan causes vibration and a flow of air, both of which are undesirable in the direct proximity of the setup, and it is connected to the LDLS by an optical fibre. Another fibre is used to connect the output of the LDLS (3) to the optical column (4) of the microscope. This optical column houses important optical elements such as an aperture for intensity regulation, a polariser and the condenser, and is used to focus the light beam onto the sample.
The transmission microscope is equipped with four objectives, all of which are optimized for long working distances. The possible magnifications are x4, x10, x20 and x60. The two objectives with the largest magnification feature an internal cover glass correction to correct for the refractive index and chromatic aberrations in the substrate glass of the

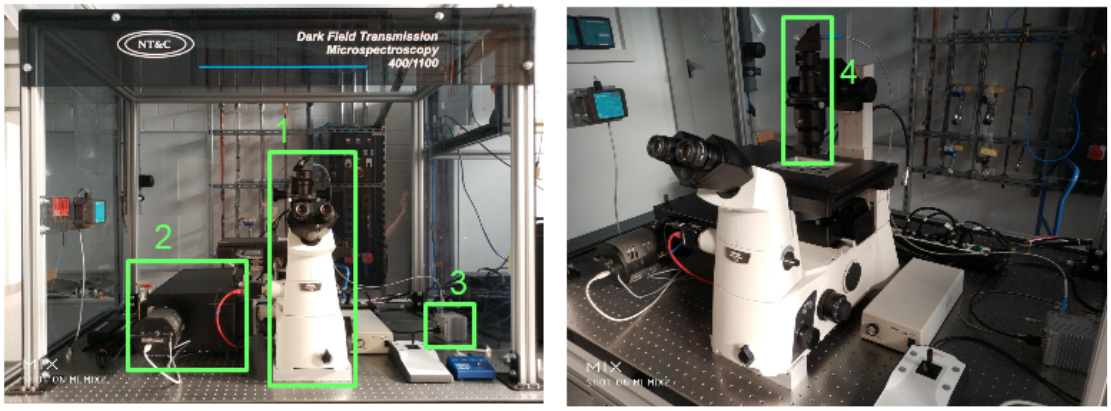

Figure 7: Photograph of the setup. Visible are the microscope assembly (1), the spectrometer (2) with attached CCD sensor, the LDLS (3) which is attached to the optical column (4) via an optical fibre.

samples.

3.2.1 Brightfield mode

The majority of measurements in this thesis are relative transmission spectra measured in bright field mode. To obtain transmission information of the structures in question, a measurement consists of two spectra: a spectrum of the structures and a reference measurement of the substrate without structures. By dividing the two, the relative transmission of the structures can be calculated. To keep fluctuations to a minimum, the reference is typically measured on the sample on a patch of empty substrate close to the structures in question.

3.2.2 Darkfield mode

In nanotechnology, dark field microscopy plays an important role due to its capability to do spectroscopy on single sub-wavelength particles. Since structure-free areas are very dark, they can not be used as references, instead a so called 'white calibration' is used. Such a white calibration (white cal) is taken on a separate sample of etched glass, which scatters light of all wavelengths evenly in all directions. Since white cal sample and structure sample do not necessarily have the same height, a single white cal is taken before and/or after the spectra of the nanoparticles have been measured, to correct all spectra in post-processing. The use of a single whit cal for all measurements comes with the disadvantage to make darkfield micro-spectroscopy very sensitive to small changes in the environment and the setup, making darkfield microscopy more challenging to use

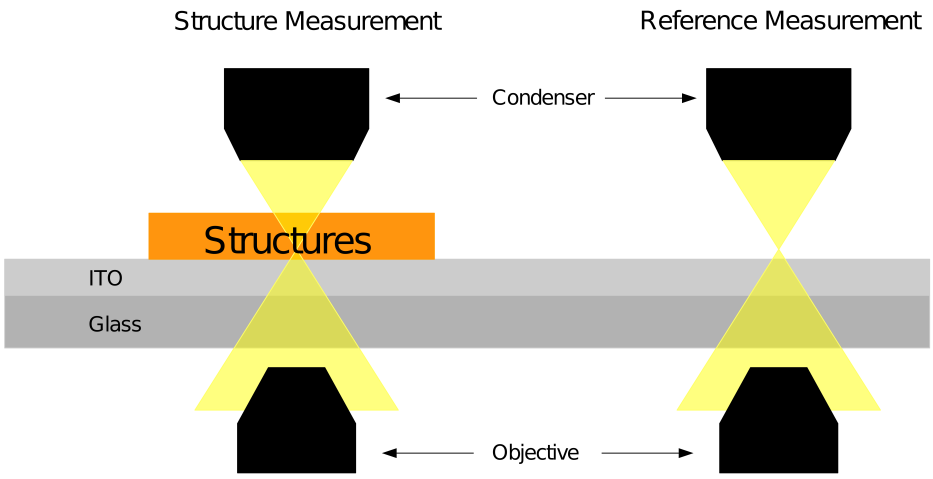

Figure 8: For relative transmission spectra, a spectrum of the structures (left) is divided by a reference (right). The two positions are typically in close proximity on the same substrate.

than the brighfield version.

3.2.3 Gas system

A sophisticated gas control system has been installed in the transmission setup. Four mass flow controllers (MFC) by Bronkhorst can be used to simultaneously control the mass flow of the connected gasses. Nitrogen, argon, hydrogen, forming gas (a mix of a small percentage of hydrogen in nitrogen), oxygen and carbon monoxide are permanently installed, valves allow the quick change from nitrogen to argon as carrier gas or the choice of either pure hydrogen or forming gas as a source of hydrogen. The system can be easily controlled from the lab computer, and can be synchronised with measurements to allow precise monitoring of the effect the gases have on the samples.
A gas cell has been designed to work in conjunction with both the gas system and the microscope to allow for full in-situ measurements in both bright field and dark field mode on up to two samples while controlling the gas mixture the samples are exposed to.

In respect to the bachelor thesis, a local kip wiki entry about the new setup was created, which contains further information on the operation of all devices. It features an in-depth explanation of all components and gives detailed information on the software as well as some trouble shooting advice. For any questions on how to use the new setup, please refer to this wiki page.

3.3 Reflection Setup

One of the samples has been measured using a reflection setup at the Max Planck Institute for Intelligent Systems in Stuttgart.

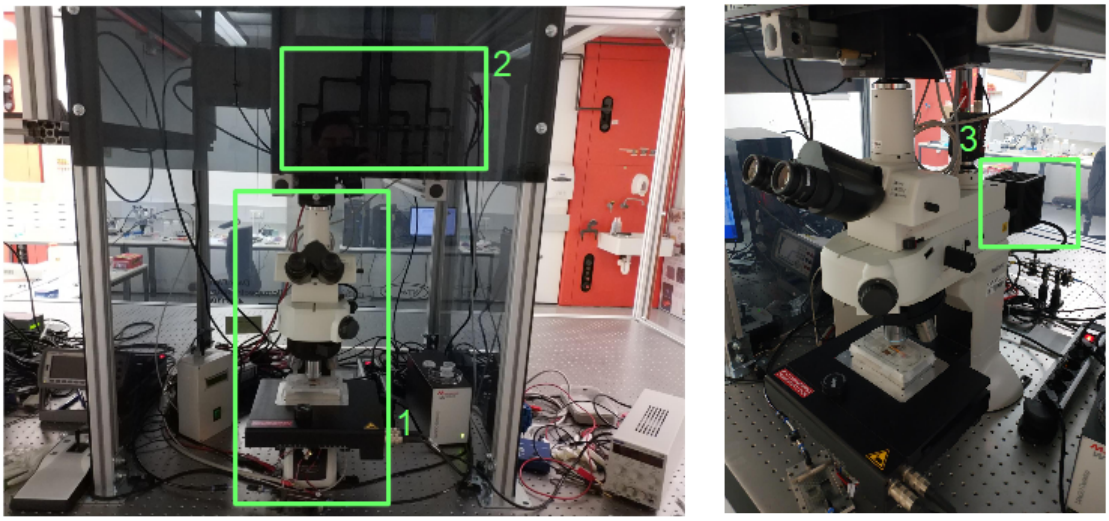

Figure 9: Picture of the reflection setup at the MPI IS in Stuttgart. (1) microscope assembly, (2) spectrometer, (3) Nikon light source

The setup is shown in figure 9, and based around a Nikon reflection microscope (ECLIPSE LV100ND) which allows for brightfield as well as darkfield microscopy. Like the transmission setup, it features a spectrometer with a cooled CCD detector by Princeton Instruments. For the measurements done for this thesis, the original Nikon light source was used. The microscope is set up with a motorized stage by Märzhäuser, and is controlled from a computer, similarly to the transmission setup in Heidelberg. Magnifications of x20, x50 and x100 are available. Due to the different geometry, the spectrometer is attached to the top of the microscope.

3.3.1 Brightfield mode

In transmission mode, the reference measurement for relative spectra could be measured directly on the sample substrate. In a reflection setup, this is not usually possible, since a highly reflective surface is needed. For the measurements in this thesis, an aluminium mirror was used. Since the mirror and the sample do not have the same height and thus require refocusing when switching between them, the same reference was used for all measurements rather than a new reference being measured each time.

3.3.2 Darkfield mode

In reflection, rather than a piece of etched glass, a small ceramic sample was used as a white cal. Other than that, the method of measuring darkfield spectra is identical to transmission.

3.4 Nanofabrication

All the samples used in this thesis have been manufactured by electron beam lithography (EBL).

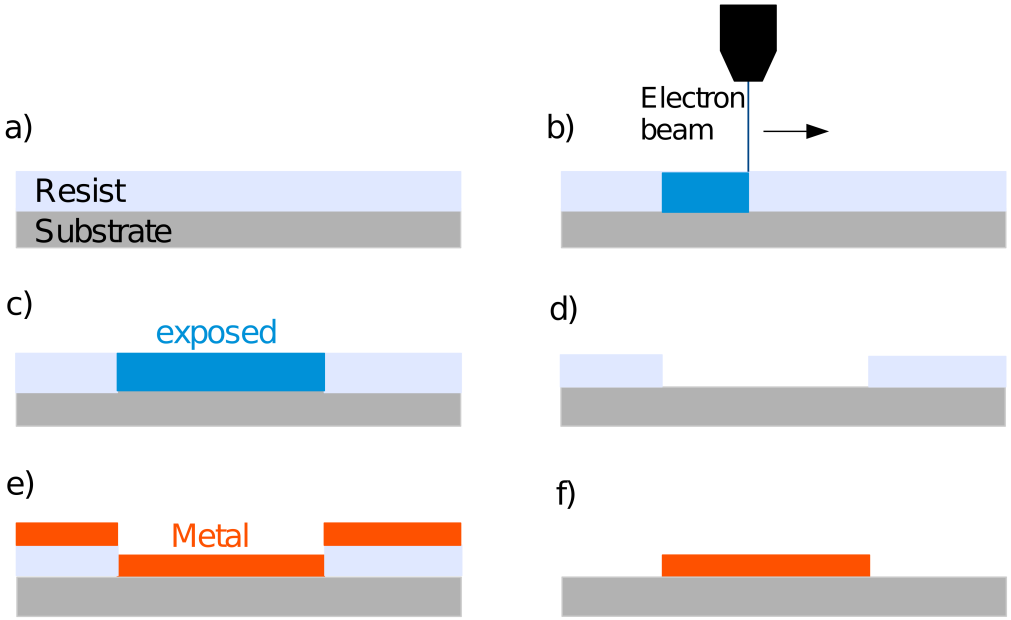

Figure 10: EBL process: a) Photoresist is spin-coated onto the substrate b) and c) an electron beam is used to expose sections of the resist d) a special solvent is used to remove all exposed resist e) the desired metal for the structures is evaporated onto the sample f) during a process called lift-off, all excess resist and metal is removed by a solvent

The steps of the lift-off EBL process using positive resist is shown in figure 10. The process begins by spin-coating a thin layer of a photoresist onto the substrate. For the samples in this thesis, PMMA was used as a resist, and substrates of glass with a thin layer of indium-tin-oxide (ITO) were used. The ITO serves as a conductive yet transparent layer to prevent charges from the electron beam to built up in the substrate during exposure, which can cause distortions in the beam. Next, the areas where structures are desired need to be exposed. Since the structures here are supposed to be below the wavelength of visible light, a beam of electrons is used. Its very small wavelength

compared to visible light allows for the manufacture of smaller structures. This exposure breaks down the long polymer chains of the PMMA, and thus makes it easier to dissolve. By putting the sample into a solvent, the exposed resist can thus be removed, while leaving the unexposed resist mostly intact. The next step in manufacture is the evaporation of metal layers onto the sample. In the final step called lift-off, the sample is submerged in a solvent, which removes all the remaining unexposed resist. This also removes all metal on top of the resist, and leaves only the desired structures behind.

3.5 Sample design

3.5.1 Gold sample DF-01

To verify that everything is in working order and that the newly installed setup reliably produces repeatable results, a calibration sample was produced. This sample, named 'DF-01', consists of well-understood gold nanostructures on an ITO-covered glass substrate. It features arrays of nanorods of varying lengths and arrays of nanodisks of different diameters, which have well-understood transmission spectra and can thus be used to check the bright field mode of the experimental setup. Furthermore, patches of isolated single nanorods and -disks have been designed onto the sample. These structures are too small and diverse to be visible in the bright field setup, but can be seen with the dark field condenser, so that its functionality can be tested. In addition to these plasmonic nanostructures, the sample 'DF-01' contains multiple structures of larger size (10µm to 100µm) to calibrate the camera image, so that sizes can be measured in the pictures taken in the Lab Control software.

Figure 11 depicts the layout of the DF-01 sample. Since this sketch does not give the full size specifications, please refer to the appended complete design specifications, beginning at page 78. The patches named 'Arrays' refer to areas with densely packed, periodically arranged nanostructures. The patches named 'single' refer to areas where the individual nanoparticles are much further apart. The array-patches can thus be seen in bright-field mode, whereas the single-patches appear invisible unless the dark-field mode is used.

The nanorods on the DF-01 sample are of a rectangular shape, all with the same width of 60nm, and varying lengths of 150nm to 240nm, with a 10nm step size. If we assume the rods to be aligned with the x-axis, in the arrays they are arranged with a centre-to-centre distance of 300nm in the y-direction, and a distance of 100nm between two rods in the x-direction. The disks have varying diameters of 40nm to 220nm in steps of 20nm. In the disk arrays, they are arranged with a centre-to-centre distance of 300nm. In the single-patches, both for rods and disks, a pitch of 10µm in both directions has been chosen, to mostly isolate the single particles from one another. Sadly, due to problems in manufac-

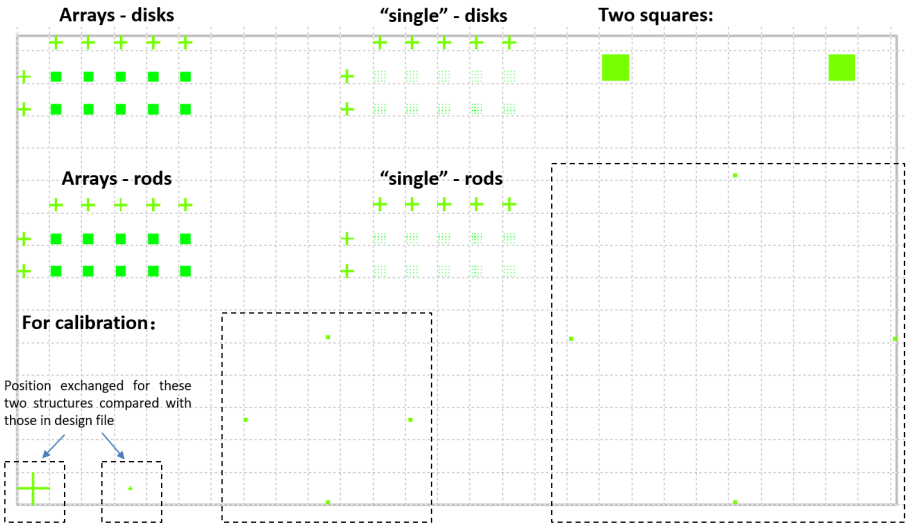

Figure 11: Schematic sketch of the layout of the DF-01 sample. The different arrays are marked, and the structures for size calibration can be found towards the right and the bottom.

ture, some of the disk-arrays were damaged, and others could not be manufactured.

3.5.2 Magnesium sample DF-02

The DF-02 sample features a very similar layout to the DF-01 previously discussed, however the arrays of disks which could not be manufactured on the DF-01 sample have been reworked, to prevent the damage seen on the DF-01 sample. Instead of gold, the structures are made of a Ti(3nm)/Mg(50nm)/Ti(5nm)/Pd(10nm) sandwich material. The titanium layer at the bottom of the stack is used to increase adhesion between the other metals and the ITO on glass substrate. The second layer of titanium between magnesium and palladium is used to prevent the alloying of the two metals, since the magnesium-palladium alloy would hinder the diffusion of hydrogen. The combination of magnesium and a palladium layer on top allows this material to display phase transitioning qualities. If the structures are exposed to hydrogen, the palladium splits the gas catalytically into hydrogen atoms which are then incorporated into the crystal lattice of magnesium. In this process, metallic magnesium transitions into the dielectric magnesium dihydride. Exposure to oxygen will catalytically oxidise the stored hydrogen and thus revert the material back to metallic magnesium.

4 Setup Parameters

4.1 Spectrum of the LDLS

In order to properly analyse any spectrum taken with the new experimental setup, a good understanding of the spectrum of the light source, its long-term stability as well as of effects caused by the optical path and the spectrometer itself is necessary to properly distinguish features in the spectrum caused by the sample from features which have a different cause. The newly installed setup has therefore been used to measure the spectrum of the LDLS and its long-term stability.

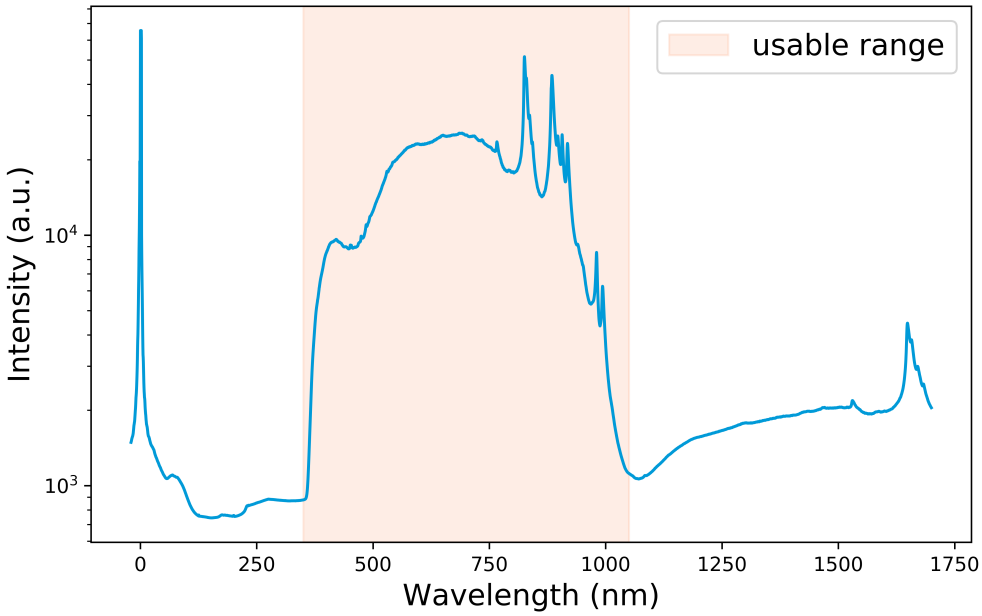

Figure 12: Full spectrum of the LDLS. Since a xenon plasma is used, characteristic lines of xenon are visible in the spectrum. The usable range is marked. AT 0nm, the zeroth order peak can be seen, at around 1050nm the second order begins.

Figure 12 shows a full spectrum of the LDLS. The spectrum was taken using the finer grating available in the spectrometer, with a grating constant of 150cm^{-1}. This grating by itself has a spectral range of about 300nm, so multiple spectra at different centre wavelengths were measured and then later on stitched together using the Data Analysis software to create this full spectrum, which covers more than the usable range. Even though the light source itself does, according to its manufacturer Energetiq, produce light

of wavelengths as low as 170nm, in our setup wavelengths below 350nm are cut off due to absorption in the glass optics of the microscope. The resulting spectrum is fairly homogeneous from around 400nm to about 900nm. Most of the spectrum resembles the shape of a black body radiator, however from about 760nm to 1000nm characteristic peaks are visible, which correspond to the characteristic lines of the xenon used as the plasma in the LDLS.
On the lower end of the spectrum, another sharp peak is visible. This peak at 0nm however is not actually corresponding to light of a specific wavelength, but rather belongs to the zeroth order. This is also the cause for other smaller peaks at very small wavelengths. In the spectrometer, a diffraction grating is used to split the light into different wavelengths, and the first order of diffraction is used. Nonetheless, the other diffraction orders are still being generated, and so on the lower end, the zeroth order becomes visible, and for high wavelengths above 1050nm the second order is detected. In figure 12, the shape of the original spectrum can clearly be identified in the second order, at the right side even the second orders of the characteristic peaks become visible again. As such, the capability of the setup is a wavelength range from 350nm, where the light from the light source first begins to have significant intensity, to 1050nm, where the second order begins. Therefore, the setup can cover the entire visible range, and a bit into the near infrared.

4.2 Long Term Stability

For long term measurements, the stability of the light source is of major importance. As was previously alluded to, most measured spectra are created by dividing the spectrum of the structures themselves by a reference. Ideally, the output of the light source would be absolutely identical at the time the reference was taken and when the spectrum of the structures was measured. To help this, both the spectrum and the reference are typically measured in quick succession. However, a real light source does always fluctuate. To quantify this effect, a long-term measurement of the light source was taken. For this measurement, multiple spectra were measured in a time frame from shortly after to around 250 minutes after plasma ignition.

The resulting long-term stability measurement is shown in figure 13, where every measured spectrum has been plotted relative to the last spectrum in this series of measurements. The spectra have been plotted with a colour range from red to white to blue. Firstly it can be noted that differences above 5% only appear in the proximity of the characteristic peaks of xenon, since at the slopes of these peaks even slight wavelength shifts cause a comparatively large difference. As can be seen from figure 13, in the first few minutes the intensity of the light source increases across the entire spectrum, and the

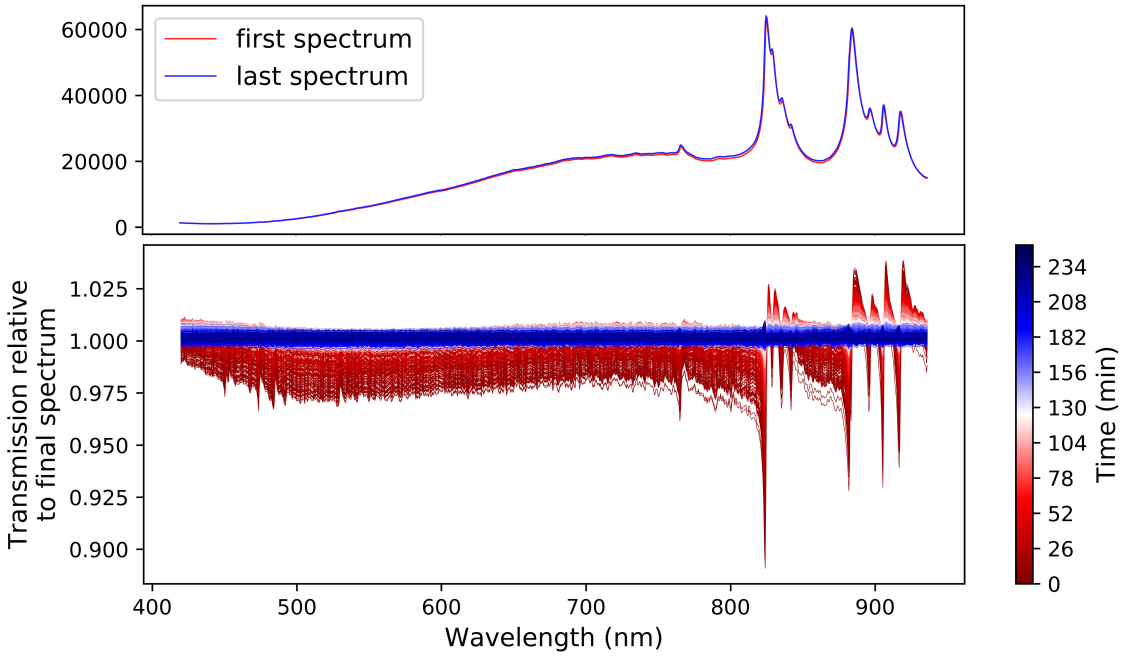

Figure 13: Stability of the LDLS. Plotted are measured spectra in a time frame from ignition of the light source to 250 minutes after plasma ignition, all spectra are relative to the last measured spectrum. The first and last spectra are plotted to ease the connection of features in the relative spectra to features in the absolute spectra. At first, the intensity increases over the full wavelength range and then stabilises. A slight shift of the characteristic peaks can be seen.

peaks blueshift slightly, which causes the peaks in the relative spectra around the peak positions.

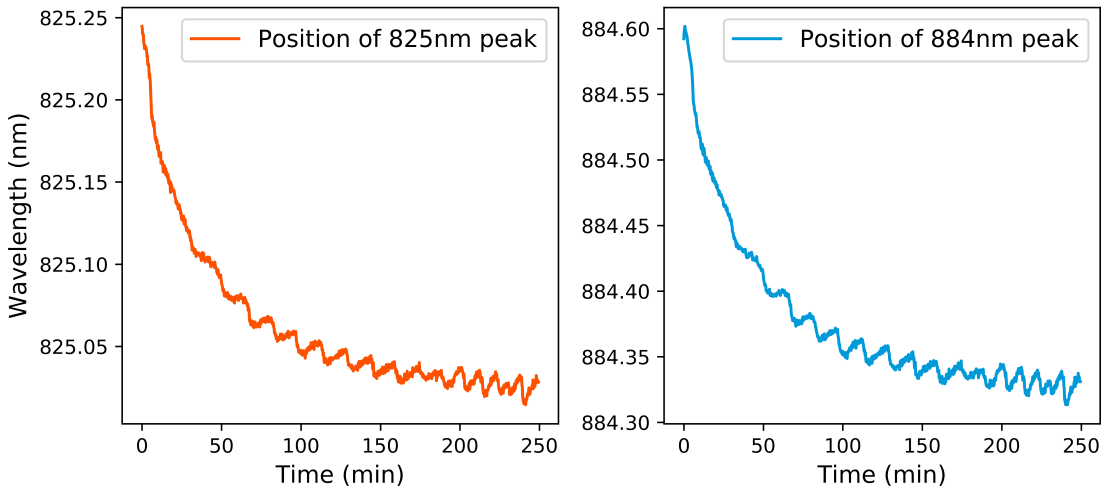

Figure 14: Positions of the two largest peaks (at around 825nm and at around 884nm) in the LDLS spectrum plotted over time. On the left: peak around 825nm. On the right: peak around 884nm. Both peaks blueshift by about 0.25nm.

In figure 14, the blueshift is much easier to see. By determining the exact position of the two largest peaks (at around 825nm and at around 884nm) in each spectrum via a Gaussian fit to the tip of the peaks and plotting them over time, the decrease in the peak wavelengths can easily be seen. From first to last spectrum, both peaks shift by about 0.25nm. The shift is most likely caused by the increase in pressure and temperature inside the lamp after the plasma ignition, and resembles exponential decay in its time-dependence.

Since in figure 13, due to the construction of the plot it is quite difficult to estimate in which time frame the most changes occur, the intensity at a wavelength of 700nm for each spectrum has been plotted over time in figure 15. Roughly 30 minutes after the plasma ignition, the deviation of the intensity from its average remains below the 0.6% threshold marked in the plot by a blue background. At first, the intensity increases rapidly, until it reaches its maximum after roughly 70 minutes. From there on, it very slowly decreases again. If a reliable measurement is to be made, one should wait for at least 30 minutes after turning on the light source to let it stabilise.

Despite fluctuations as large as 0.6% in this measurement, it needs to be kept in mind that typically less than a minute or a few minutes at most pass between the measure-

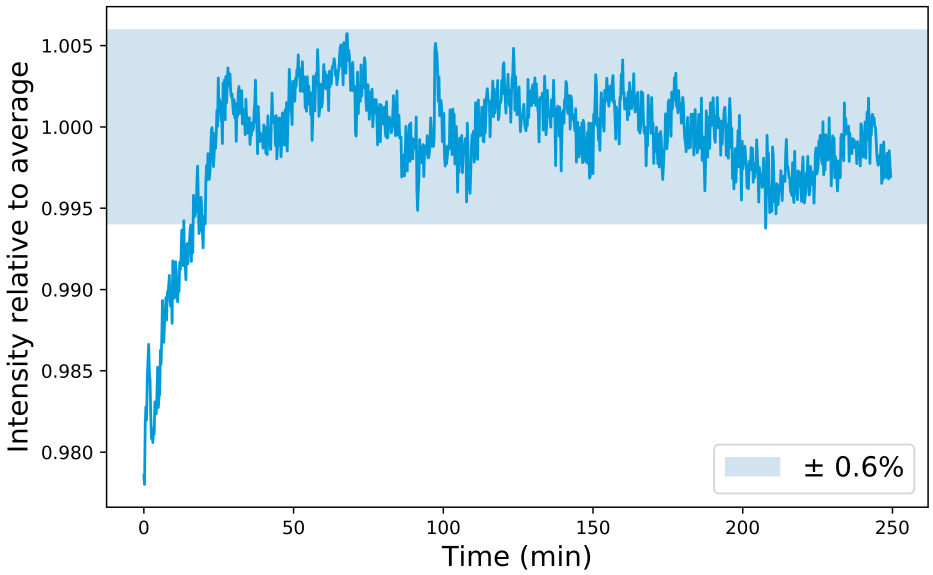

Figure 15: Intensity at 700nm of the LDLS spectrum over time. The coloured background resembles a region of ±0.6% around the average. After roughly 30 minutes, the light source reaches is maximum stability.

ment of a spectrum and the measurement of the corresponding reference. At time intervals between a measurement and its reference of 14s to 120s, an average deviation in the intensity of the light source at 700nm of less than 0.15% can be deduced from the measurements above.

4.3 Unity Line

Measuring a spectrum and referencing it against itself does also offer valuable insight into the quality of measured spectra. Deviations in the performance of the light source as well as the spectrometer itself are going to affect these measurements just like they would influence other measured spectra, and since by referencing a spectrum against itself a constant value of 1 would be expected, these deviations become more clearly visible.

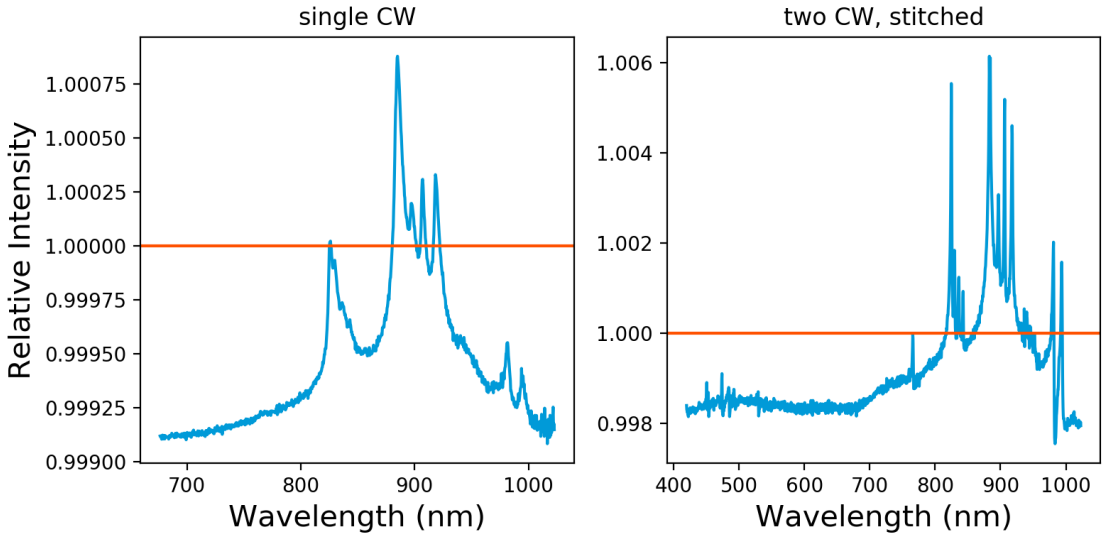

Figure 16: Measurement of a reference against itself. In an ideal setup, it would be constantly 1. On the left: Unity line for a single centre wavelength (CW) (no stitching needed). On the right: measurement at two different centre wavelengths, stitched together to create a wider range spectrum. Stitching decreases the smoothness, as deviations from 1 are much larger.

Such a measurement is show in figure 16. In orange, an ideal result of continuously 1 is depicted. This type of experiment has been done for unstitched spectra, where only a single spectrum at a single centre wavelength (CW) was measured (seen on the left), as well as for measurements with stitched together spectra to increase the overall spectral range (seen o the right). For the unstitched case, values range from 0.999 to 1.001, with the maximum value being encountered around the xenon peaks. In the stitched case, the

overall shape is very similar, however the values range from 0.998 to 1.006, noticeably exceeding the values obtained for the unstitched unity line. Since values close to 1 are desired here, it is preferable to use spectra without stitching to improve overall quality. This does however come at a significant loss of spectral range, so the proper setting has to be chosen for a given application.

4.4 Polariser

As was previously alluded to, asymmetric structures such as rods have different excitation modes along different directions. Polarised light can then be used to only excite a very specific one of these modes, which is why polarisers are an essential part to research asymmetric nanoparticles. To calibrate the polariser of the setup, measurements on nanorods and nanodisks under different angles of polarisation were taken.

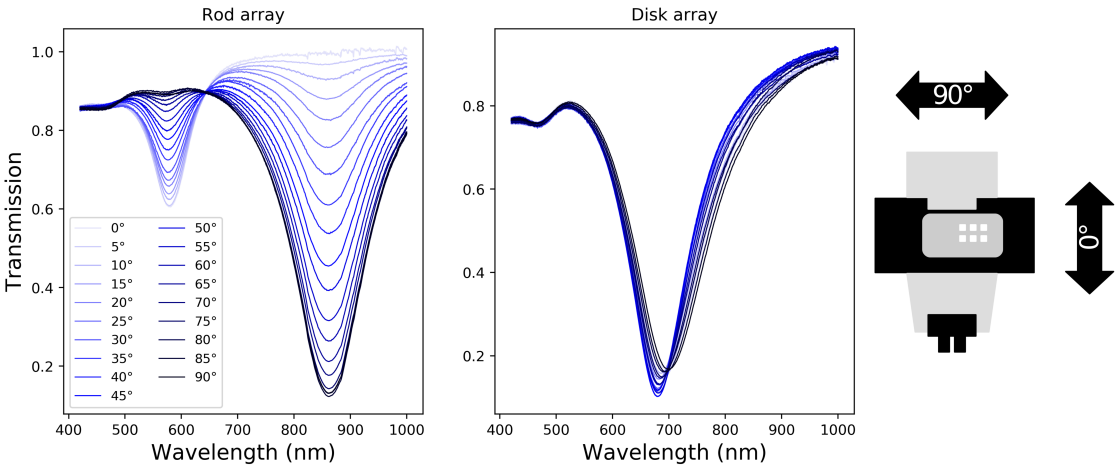

Figure 17: Transmission of rods (left) and disks (right) with different polariser positions (schematic top view of microscope on the right). The asymmetric properties of rods and symmetric behaviour of disks can be seen.

This measurement can be seen in figure 17. As expected, the orientation of the polariser directly affects the amplitude of the modes for the rods. To excite a specific mode, a light component along the direction of the mode is required. If the light is therefore polarised along the direction of the specific mode, its amplitude will be maximal. If the light is polarised perpendicular to it, the mode can not be excited and the amplitude will thus be zero. Since this behaviour is well visible in the measurement above, the polariser functions as expected. The data can also be used to find out which polarisation direction corresponds to the 0° position. This has been depicted in figure 17 on the very right with a schematic representation of the microscope seen from above.

Just like the rest of the setup, the transmission of this polariser has to be measured as well to understand its behaviour before using it for measurements on samples. Ideally, a polariser would filter light evenly across all wavelengths, but in reality this is not the case. The transmission of the polariser at an orientation of 0° as well as orientations of 45°, 90°, 135° and 180° have been measured, and were referenced against a long-term measurement of the LDLS.
Ideally, the absorption spectra of the different orientations of the polariser should be identical, since an unpolarised light source is used. It should also be noted, that in order to install the polariser, multiple components in the optical path have to be disassembled. During this dis- and reassembly one can easily accidentally change adjustments to the aperture or focus of the beam, which will affect the light intensity. As such, the relative absorption spectra of the polariser may be offset slightly. For most measurements however, the shape of the spectrum is the major concern, which should be unaffected by the installation process.

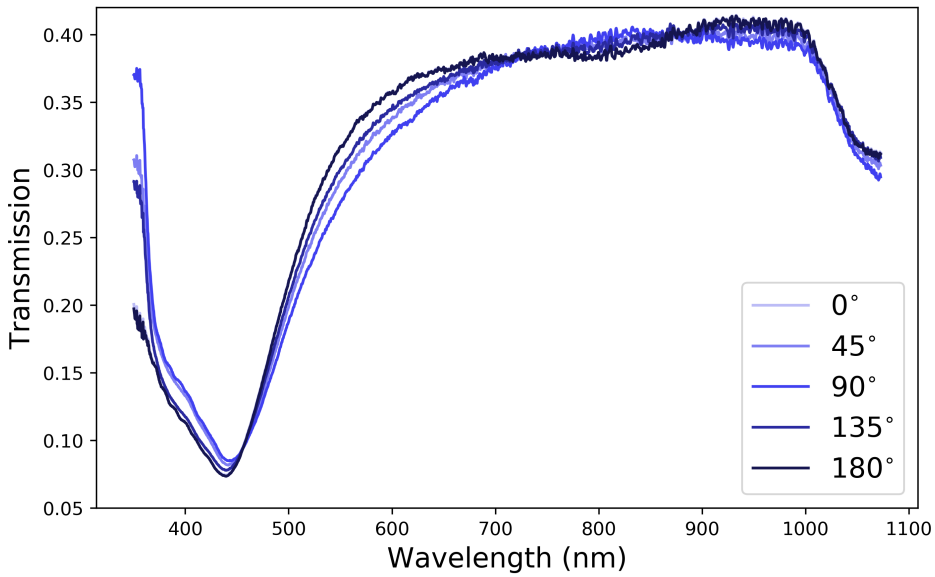

Figure 18: Relative absorption spectra of the polariser at multiple orientations between 0° and 180°. A consistent absorption from 600nm to 1000nm is apparent, with a significant dip around 450nm.

The relative absorption of the polariser is depicted in figure 18. From 600nm to 1000nm it has a fairly consistent absorption, but it does have a considerable dip at $\sim$ 450nm. This needs to be kept in mind if phenomena in this wavelength range are to

be researched, since it noticeably reduces the available intensity. In the constant range the polariser's transmission is roughly 40%, and the spread of the spectrum at different orientations is reasonably small. Since the orientations of 0° and 180° are supposed to be equivalent, it is not surprising that the spectra for these two orientations mostly overlap.

5 Measurements in transmission

The results presented here concern the DF-01 gold on ITO/glass sample, and were taken using the transmission setup. At first, to verify that the sample matches the design specifications, a scanning electron microscope (SEM) was used to take images of the structures.

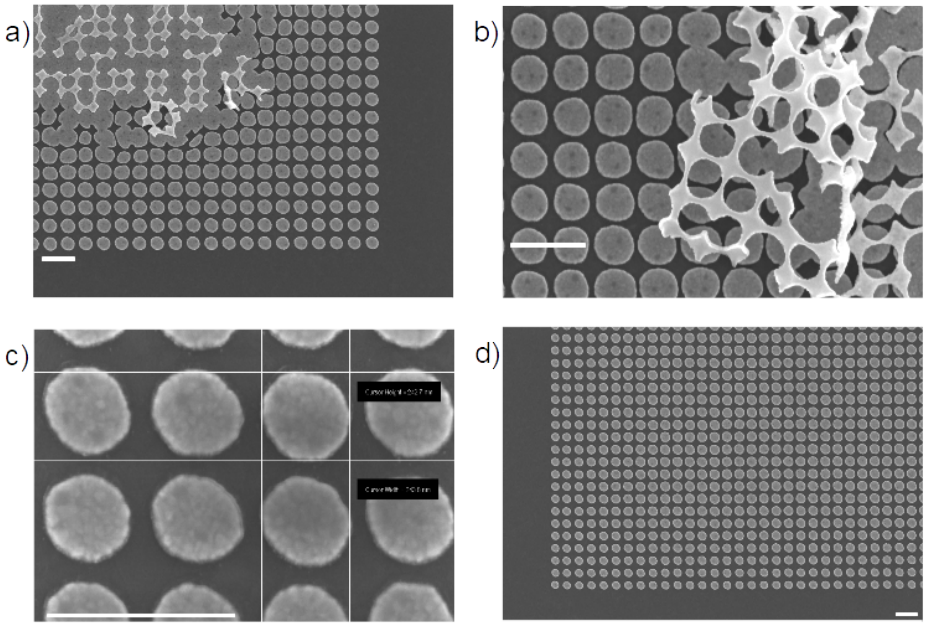

Figure 19: SEM images of the disk arrays of DF-01. Pictures a) and b) depict the damages of the arrays with larger disks, c) is a close-up of undamaged disks with a size measurement, and d) shows the image of an array with visible diameter shift. All scale bars are 500nm.

Figure 19 depicts some of the images taken of the disk arrays. As previously mentioned, some of the disk arrays were damaged during manufacture, as can be seen in images a) and b). It is visible how towards the centre of the array, the disks begin to 'grow together', and how the lift-off did not work satisfactorily. A possible explanation for this might be an effect called 'proximity effect' in electron beam lithography, where due

to scattering of electrons, areas around the incident spot are slowly exposed. If dense patterns like in this case are written, the accumulated exposure due to this proximity effect can cause areas to be exposed which were originally not intended for exposure. This may have caused exposure of the area between the disks, which would result in the disks growing together. It may also explain why even in the undamaged arrays, an increase in disk diameter towards the centre of the array can be detected. The centres of the arrays are more prone to damage by proximity effects, since a large area around them has been densely exposed, leading to high accumulation of undesired exposure.

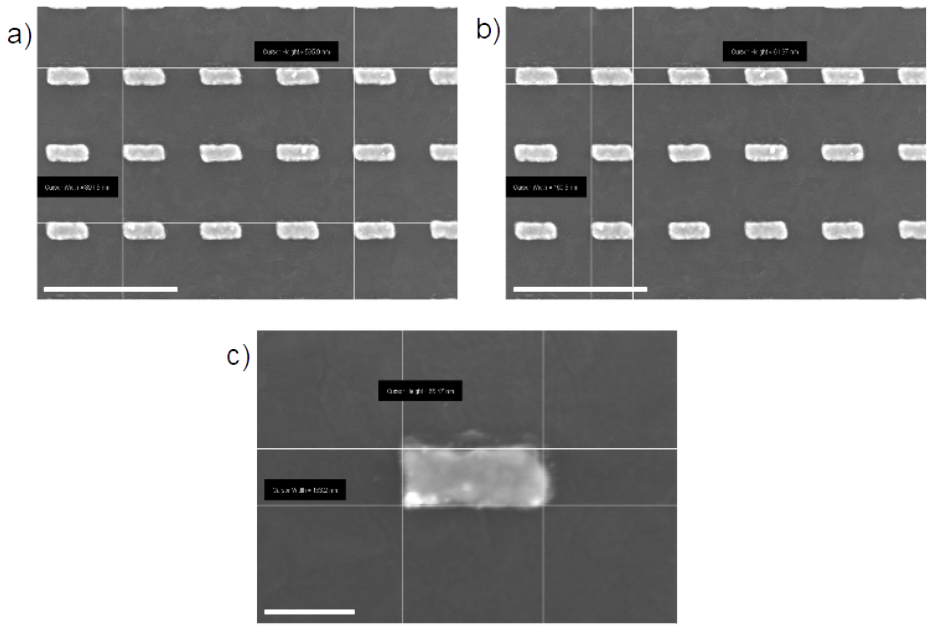

Figure 20: SEM images of the rod arrays of DF-01. Pictures a) and b) depict arrays of rods with measurements on size and periodicity, c) is a close-up of a single rod. Scale bars: a) and b) 500nm, c) 100nm.

Similar pictures of the rod arrays have been taken and can be seen in figure 20. Luckily, all rod patches were manufactured completely and without damage.
In general, the size measurements in the SEM images has shown that errors in the sizes of about $\pm$5nm have to be expected on the DF-01 sample.

5.1 Spectra using unpolarised light

First, spectra of the rod arrays using unpolarised light were taken. The measured spectra are all relative to a reference spectrum taken at a structure-free location on the ITO on glass substrate, and were taken using the bright-field condenser.

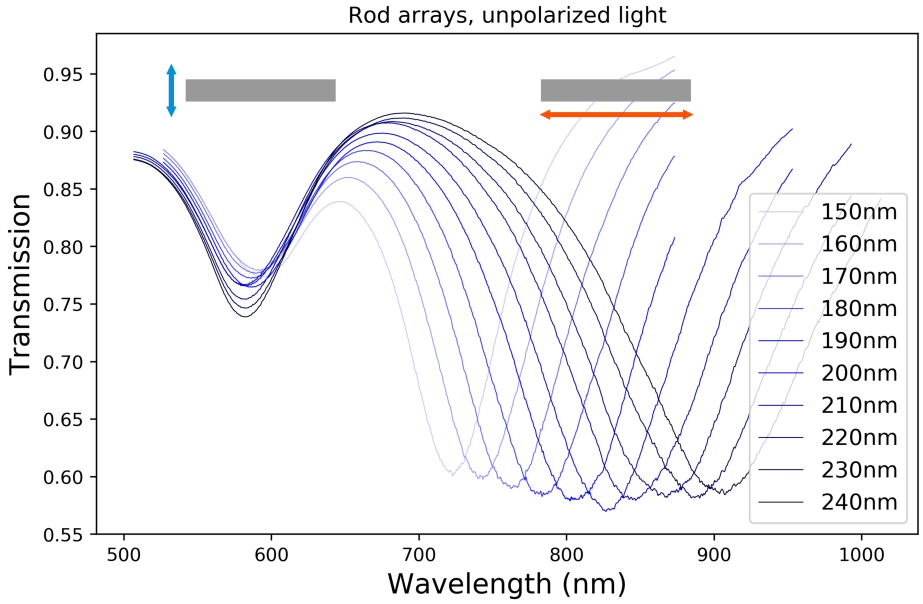

Figure 21: Spectra of the arrays of nanorods. All rods have a width of 60nm, lengths differ from patch to patch and are given in the legend. The two resonances are well visible. The parallel mode redshifts for longer rods.

The resulting spectra can be seen in figure 21. The centroids of each peak was calculated to determine the spectral positions (see appendix B for details). Even on first sight, it is visible that there are two peaks in each spectrum. This is a simple result of the geometry of the nanoantennas: since the nanoantennas are of a rectangular shape with different length and width, two different resonances can be excited. One resonance along the long axis of the antenna, called the 'parallel' mode, and a resonance along its width, called the 'orthogonal' mode. To excite a mode along a given axis, an oscillating electric field in the same direction is required. Since here however we have used unpolarised light of normal incidence on the structures, the electric field has components in both the parallel and the orthogonal direction, and thus both modes can be excited.
It is also visible that the peak at longer wavelengths, which can be associated with the parallel mode, redshifts more and more for longer antennas, whereas the smaller peak at lower wavelengths, corresponding to the orthogonal mode, experiences a slight blueshift. This can easily be understood if we approximate the nanoantennas as elongated spheroid particles. This is of course a rather crude approximation, since the antennas are of a rectangular shape, but as was explained in the theoretical background, no analytical description of the resonance behaviour of rectangular particles exists. As such, elongated spheroids are the closest possible approximation with an analytical solution. This description was introduced in the chapter on particle plasmon polaritons, where a graphical representation of the behaviour of the parallel and orthogonal resonance position was given in figure 4. From this result, for increasing spheroid length, a linear increase in the wavelength position for the parallel mode, and a convex decrease of the resonance wavelength of the orthogonal will be expected. To compare the measurement on the arrays to the theoretical expectations, the peak positions derived by centroid calculation of the measured spectra were used.

Figure 22 depicts the resulting plot. As expected, a very linear behaviour of the peak position of the parallel mode can be seen. Also, while not quite as closely resembling the shape anticipated by Gans-theory as the parallel mode, the orthogonal mode decreases convexly. Comparing the absolute values provided by the analytical description with the measured results is not strictly possible, due to the approximations we made. First of all, the shape of the antennas does not actually resemble the spheroid shape assumed here. In addition to this, the dielectric function was approximated by the Drude-model with all dampening being neglected. As such, the absolute results vary noticeably from the measured data, and the theoretical description only serves as a qualitative explanation for the general behaviour.

The same measurement with unpolarised light has also been done on the arrays of disks. Due to the aforementioned problems during manufacture, only five of the intended

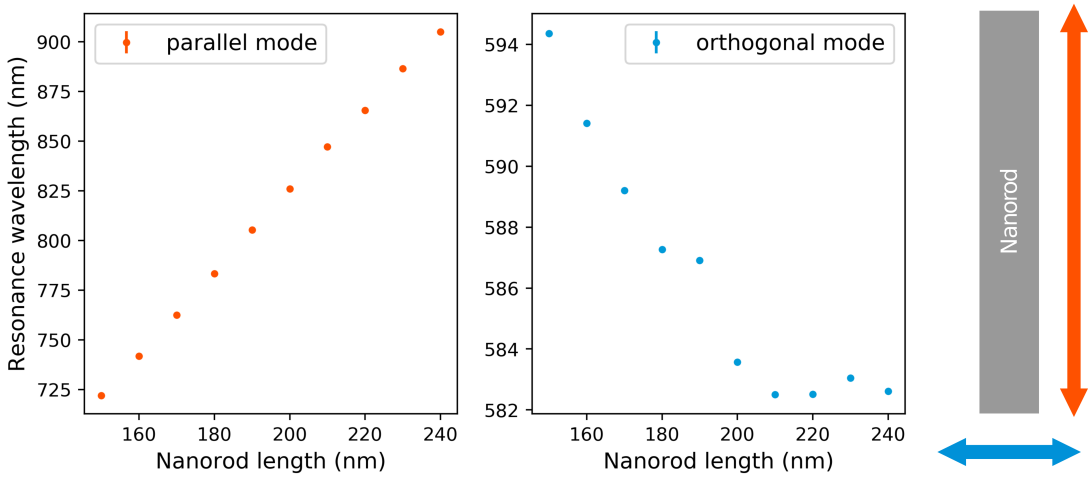

Figure 22: Shift of the spectral positions of the resonances of the parallel mode (left) and the orthogonal mode (right). The parallel resonance increases linearly with rod length, whereas the orthogonal mode decreases convexly. The parallel mode shifts more severely than the orthogonal mode.

ten arrays were produced. The spectra of the nanodisks can be seen in figure 23. Since the disks are of rotational symmetry, for normal incidence of light only one mode can be excited. Just like before for the nanoantennas, the peak positions were determined by calculating the centroids. Despite the significant damages to the structures, dips in the spectrum are still recognisable, they may however not be caused by plasmonic resonances. In general, the increasing grade of damage to the disks with increasing diameter can very well be seen. The smallest disks depict a very pronounced resonance, as would be expected. However, the resonance peaks become less and less pronounced as the disks increase in diameter, indicating the increasing amount of damage to the nanostructures. For the two largest diameters, it can be seen that especially towards the bluer end of the spectrum, the transmission in general is comparatively low, even at wavelengths where no resonance should cause a low transmission. This is caused by the very dense coverage of the gold. As can be seen in the SEM-pictures of the disks in figure 19, the lift-off on the latter structures did not work properly, causing a near complete gold-coverage towards the centre of the arrays. The broadening of the resonance peak which can be seen in the spectrum of the array of disks with a 160nm diameter is caused by the varying size of the disks that were actually produced. In this array the accumulation of the proximity effect did not yet cause the lift-off process to fail, but it did cause the disks towards the centre of the array to have an increased diameter compared to the disks at the array's

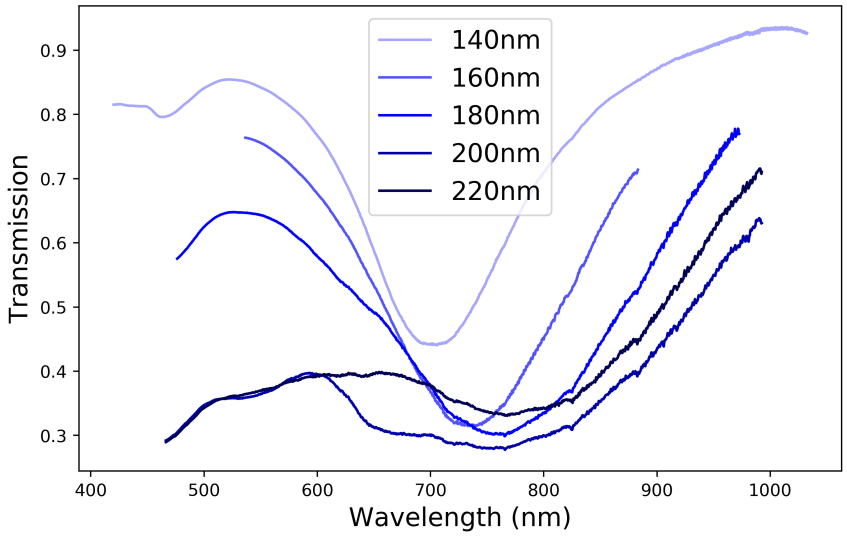

Figure 23: Spectra of the disk arrays. The diameter of the disks in an array are given in the legend. Due to the damage on the larger arrays, they depict wide ranges of high absorption rather than clear resonances.

perimeter. This causes slightly different resonance wavelengths of the disks in the array which then overlay and form the widened resonance peak visible in the spectrum.

Nonetheless, like before, the diameter dependency of the resonance wavelength as determined by the calculation of the centroid has been visualized in figure 24. The minimum transmission T_{min} was calculated as the value at the centroid position. The maximum extinction E_{max} at the dip is then given by:

$$E_{max} = \ln\left(\frac{1}{T_{min}}\right) \tag{48}$$

The peak extinction has also been plotted in figure 24. A general increase in the resonant wavelength is visible despite the damaged structures. The peak extinction increases due to the increasing absorption which is mostly caused by the array centres growing together.

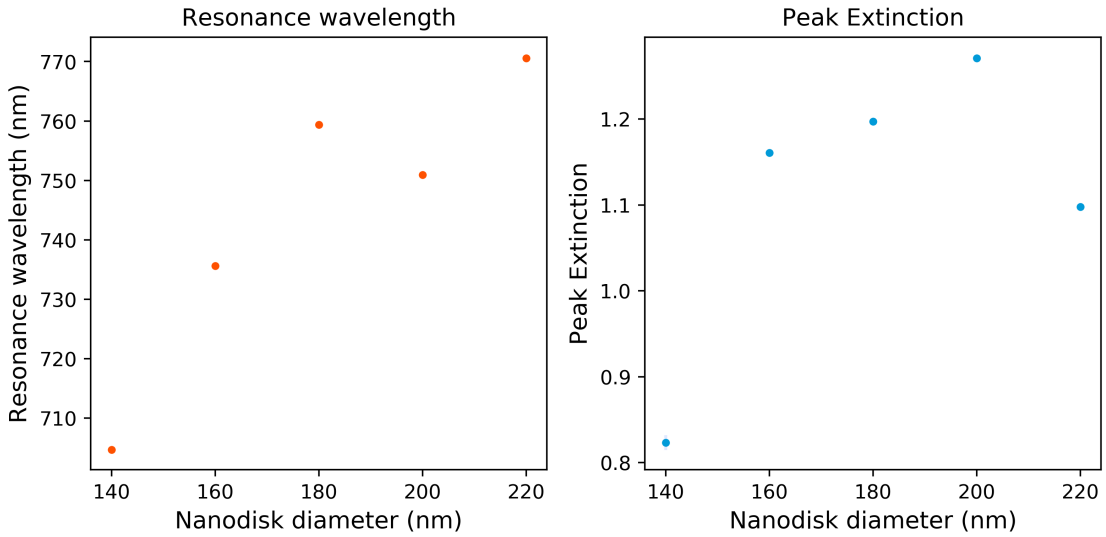

Figure 24: Resonance wavelengths and peak amplitudes of the extinction of the nanodisk arrays versus disk diameter.

5.2 Spectra using polarised light

In the spectra of the nanoantennas, the two separate peaks are caused by plasmonic excitations along different axis of the nanoparticles. Since an electric field component in the direction of an axis of a resonance is needed to excite it, polarised light can be used to selectively excite a specific resonance. Other than the use of a polariser, this measurement is identical to the one above, where unpolarised light was used.

The spectra of the rods taken with polarised light to excite the orthogonal mode is shown in figure 25. As expected, only one peak per spectrum is visible. By comparing to the spectra taken using unpolarised light, this peak can indeed be identified as the shorter wavelength peak associated with the orthogonal excitation mode. Again, the centroid for each peak was calculated. In this depiction of the spectra, it is well visible that the peak position blueshifts slightly with increasing rod length, and that its intensity increases.
The very same measurement has been repeated with light polarised to only excite the parallel mode.

Again, only one peak is visible, and this time it can be identified as the resonance of the parallel mode. It can be seen that for increasing rod lengths, the peak redshifts, and does so much more noticeably than the orthogonal mode. As with the orthogonal mode, the intensity increases with the rod length, however not quite as much. To make this more apparent, the peak positions and amplitude will be compared.
First, we will consider the peak positions, similar to the previous case with unpolarised

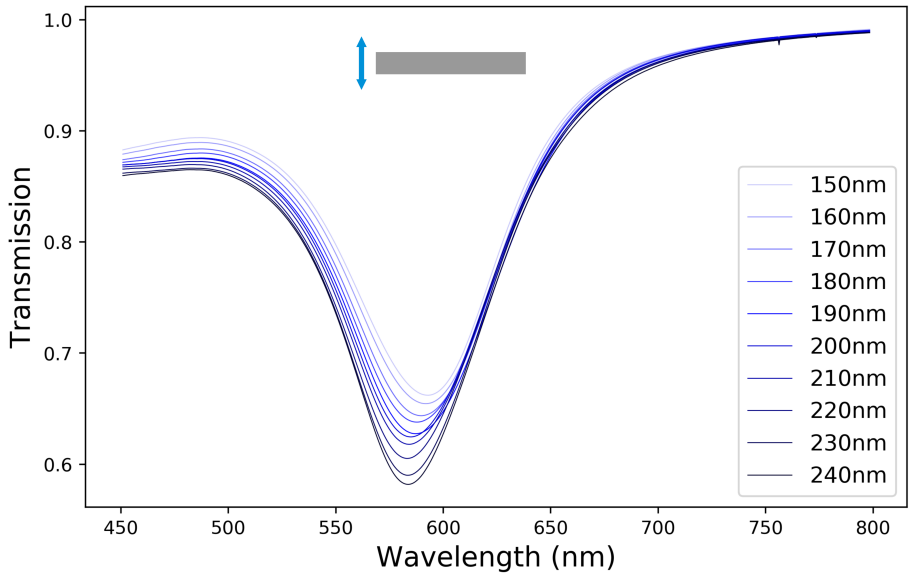

Figure 25: Relative spectra of the nanorod arrays, using polarised light to excite only the orthogonal mode. It can be seen how the peak extinction increases with the rod length, while the spectral peak position decreases.

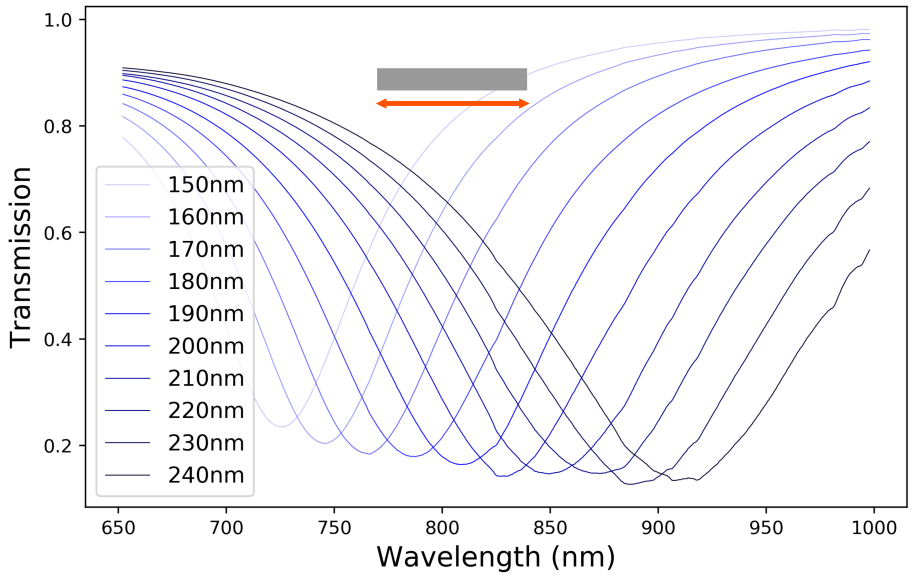

Figure 26: Relative spectra of the nanorod arrays, using polarised light to excite only the parallel mode. It can be seen how the peak extinction and spectral peak position increase with the rod length.

light.

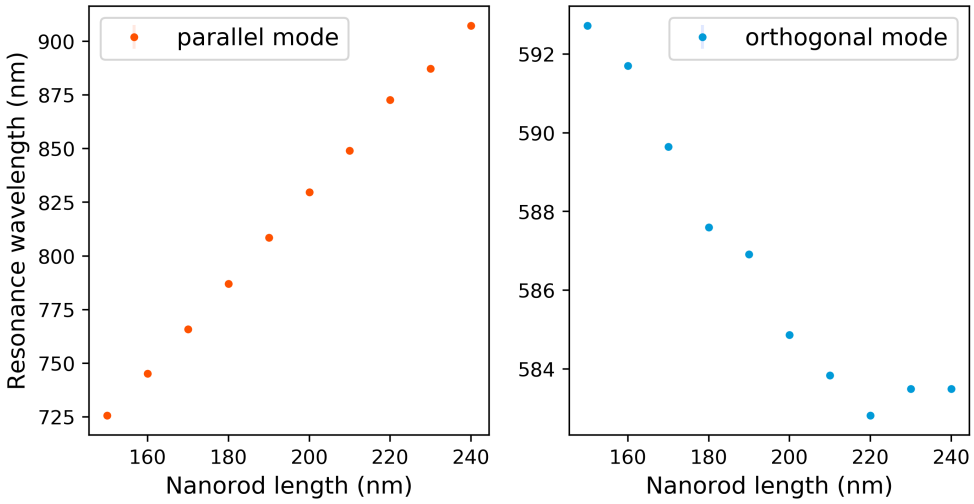

Figure 27: Peakshifts of the two resonances. On the left, the parallel mode is shown. On the right, the orthogonal mode is depicted. The linear behaviour of the parallel mode is well visible, and so is the convex decrease of the orthogonal mode.

As expected, this shows the very same results as previous measurements with unpolarised light. As predicted by Gans-theory, a linear increase in the resonance wavelength for the parallel mode can be observed, while the orthogonal mode blueshifts for longer rod lengths. Next, the peak intensities have been plotted over the rod lengths.

This plot can be seen in figure 28. From the spectra of the nanorod arrays taken using the polarised light, spectra 25 and 26, a general trend for higher extinction with increasing rod length could already be seen. In this representation, this behaviour becomes even more clear. The extinction of the orthogonal mode increases somewhat linearly, the extinction of the parallel mode shows a more noisy profile. Over the rod length range used here, the extinction of the parallel mode increases by about 10%, and in the case of the orthogonal mode by about 8%. This is simply due to the increasing size, and therefore increasing number of electrons, within the nanoantennas, as well as the increasing coverage. A larger number of electrons for the plasmon polariton excitations increases the magnitude of the resonance, and with increasing rod size, the relative area covered by the rods compared to the array's area also increases, which also enhances the extinction.

The disk arrays have also been measured using polarised light. However, since they have full rotational symmetry, the use of polarised light has no effect on the resulting

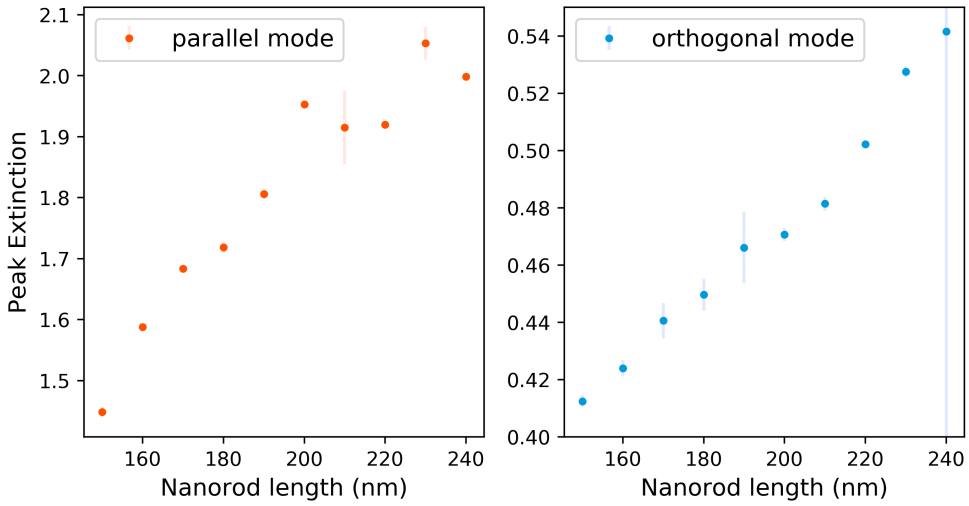

Figure 28: Peak extinction of the parallel (left) and orthogonal mode (right). For both modes, the extinction increases linearly with the rod length.

spectra, other than the fact that the usable spectral range decreases due to the short wavelength absorption of the polariser.

5.3 Darkfield mode

As was previously alluded to, dark field microscopy allows to do spectroscopy on single sub-wavelength particles. To test the dark field mode, single rods and disks were manufactured onto the DF-01 samples. The 'single' designation refers to 16 (4x4) particles of a certain type and size, arranged with centre-to-centre distance of 10µm between them. At these distances, the particles do not interact, and can therefore be treated as single individual particles. Due to the low coverage in these patches, they are invisible in bright field mode. For each of the single-patches, 4 particles were measured.

For the disks, the single particle spectra can be seen in figure 29. The sudden change in peak intensity between the disks of 140nm diameter and 160nm diameter are caused by the use of a different white calibration, which was necessary due to changes in the parameters used for the measurements. This indicates how sensitive darkfield measurements are to the calibration: Even minor changes in the light source intensity, spectrometer slit width or other parameters can have a significant effect on the results.
Especially the disks of 60nm, 140nm and 160nm depict a very clear, single peak, as is expected for the disks. The larger disks show broadened peaks, and some of the smaller peaks like the 80nm and 100nm disks seem to display two slightly offset peaks, which

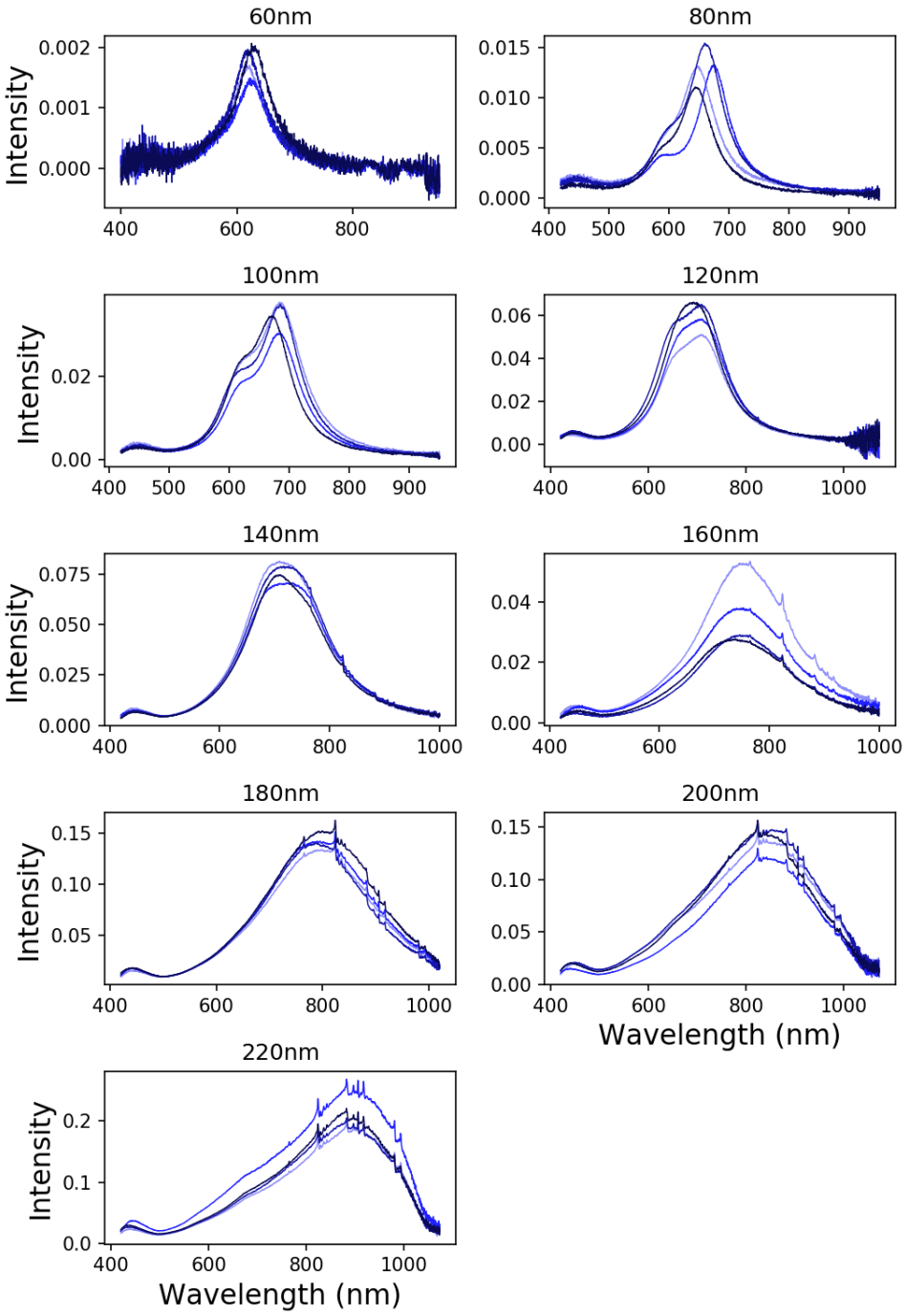

Figure 29: Single particle spectra of the disks on the DF-01 sample. For each size, the spectra of four particles were measured. It can be seen how with increasing particle size, the resonance wavelength and maximum intensity increase as well.

may be caused by astigmatism of the structures. If they are not circular in shape, but elliptic, then two different excitation modes (similar to the nanorods) would be visible.

For particles of equal size and shape, identical resonance spectra would be expected. However, darkfield microscopy on single particles is a very sensitive method of spectroscopy, and small changes in the setup such as light source intensity, ambient light or spectrometer slit width can have a noticeable effect on the measured intensities. Additionally, as was previously discussed for the SEM images of the sample (figures 19 and 20), manufacture of nanoscale structures is very difficult, and thus comes with unavoidable inconsistencies in the exact sizes of fabricated structures.

The same was repeated for the single rods. Since unpolarised light was used for the measurement, both the parallel and perpendicular mode are expected to be visible in the spectra.

As expected, in the spectra of the single rods (figure 30), two peaks are visible. The parallel mode, at higher wavelengths and intensities, is clearly pronounced in all spectra, and at lower wavelengths a second peak is visible, which can be associated with the perpendicular mode. It is however also visible that the perpendicular mode is much weaker and less sharply pronounced as in the measurements on the arrays. Similar to the disks, the different spectra of similar particles do deviate from one another, which is caused by fluctuations in the particle dimensions. As the particle size increases, the overall intensity of its scattered light increases as well, which agrees with theoretical models.

Again, the peak positions were determined by centroid calculation. Since the structures were manufactured with the same specifications as the corresponding equivalents in the arrays, the peaks should roughly be at the same spectral positions.

In figure 31, the peak positions of the single rods are compared to the peak positions previously measured in bright field mode on the rod arrays. In general, the peak positions of the single structures (blue) are redshifted relative to the arrays. For the parallel mode, the difference is smaller for short rods, and increases with the rod length. For both single and array structures, a linear behaviour of the parallel resonance with the rod length is visible, however this correlation seems steeper for the single structures. For the perpendicular rod, a large constant offset of $\sim$ 50nm can be seen.
These deviations are caused by interactions between the rods in the arrays (see [8]). Since the rods in the arrays are separated by distances of only 300nm, they do interact with each other, causing the resonance positions to shift. As expected, the general dependency of the resonances on the structure size is similar for the single- and array-structures.

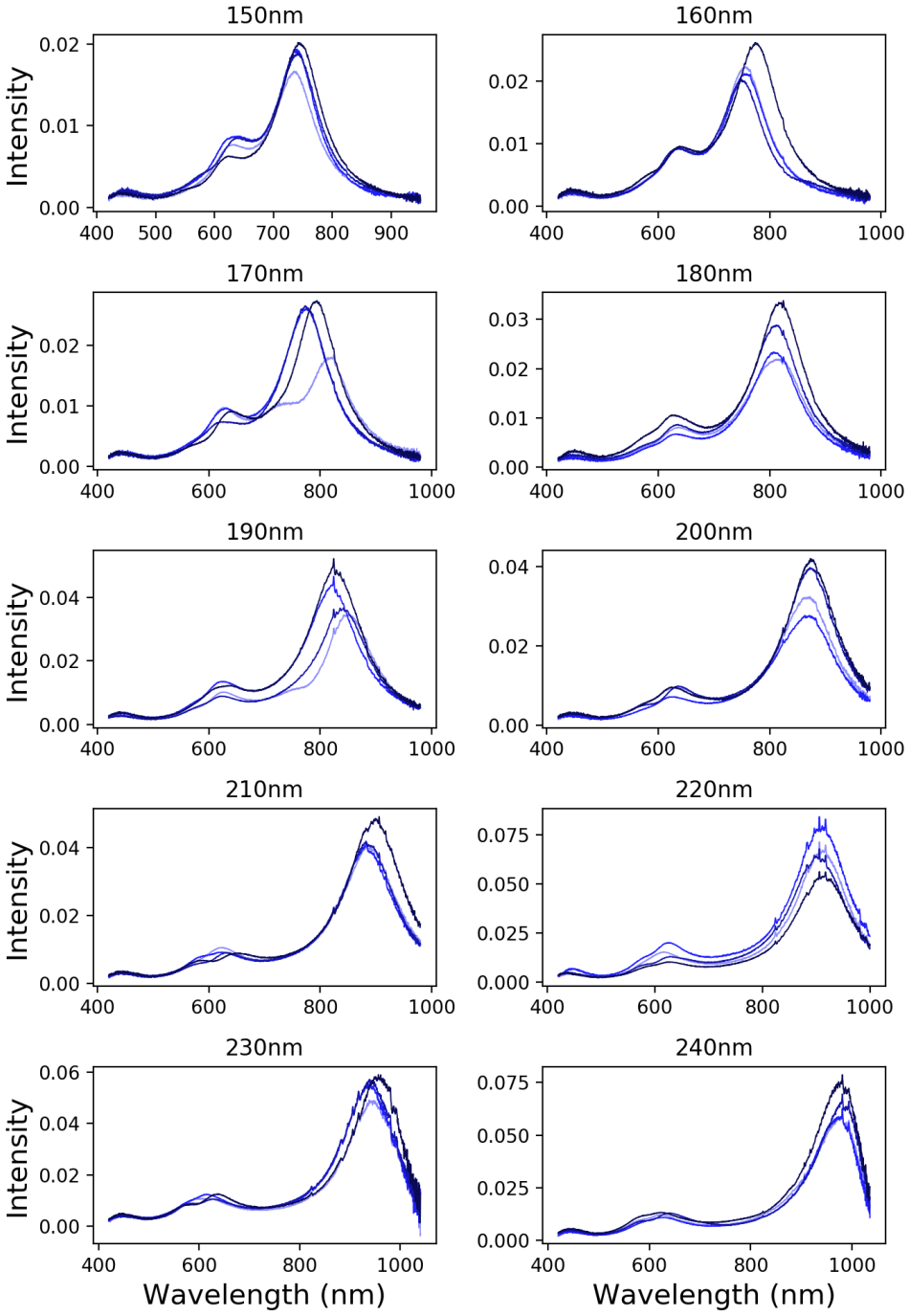

Figure 30: Single particle spectra of the rods on the DF-01 sample. For each size, the spectra of four particles were measured. The two modes are well visible, and so is the increase of peak position and amplitude with rod length.

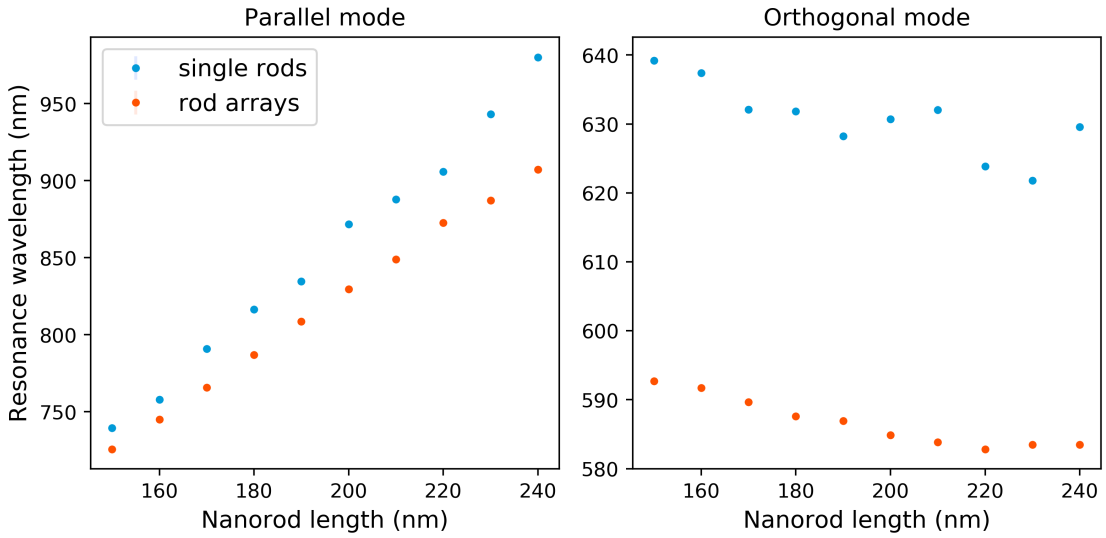

Figure 31: Shifts of the parallel (left) and orthogonal (right) mode of nanorods. In blue, the data from the darkfield measurements on single particles is shown. In orange, the data using brightfield mode is depicted. The deviations are caused by interactions between individual particles in the arrays.

6 Measurements in reflection

To properly use data from the new setup, it is very helpful to know how its measurements compare to other experimental installations. For this purpose, the DF-01 gold sample was measured again using a reflection setup at the MPI IS in Stuttgart. Since however the DF-01 sample was originally designed for transmission, and thus made on a transparent glass/ITO substrate, it is not ideal for reflection, where typically much more absorbing substrates such as silicon are used.

6.1 Brightfield mode

Just like before, in brightfield mode spectra of the arrays were measured using both unpolarised light.

6.1.1 Spectra using unpolarised light

First, upolarised light was used. Since the disk arrays on the DF-01 sample were largely damaged, the reference measurements focused on the rod arrays

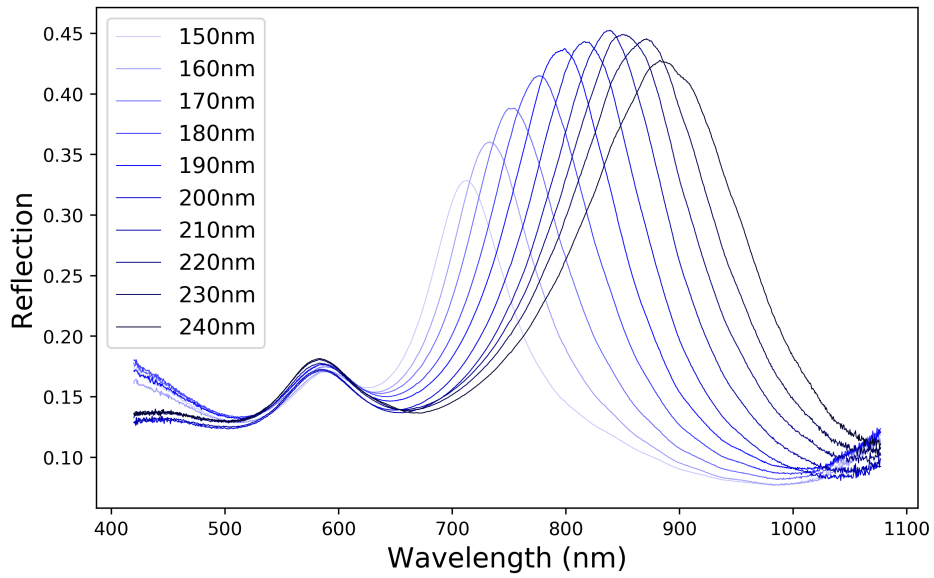

Figure 32: Rod arrays in brightfield in reflection. As expected, both modes are visible. Opposed to transmission, a resonance is visible as a peak rather than a dip. The shift of the peak position with the rod length can clearly be seen.

The spectra of the rod arrays are shown in figure 32. Since unpolarised light is used, both the parallel and perpendicular modes are visible. When comparing these reflection spectra to the ones measured in transmission, it is immediately visible that the resonances are now peaks, where the intensity is higher than the background, as opposed to transmission mode, where the resonances cause a dip with lower intensity.
In the transmission spectra, with increasing nanorod length the amplitude of the resonance increased linearly and evenly. Even upon first gaze, this behaviour is not present in the reflection spectra. Instead, for the parallel mode at higher wavelengths, the amplitude first increases, reaches its maximum at 210nm rod length and from then on declines for longer rods. Nonetheless, the peaks are well pronounced, and thus a comparison of the peak positions can be made. However, to increase the intensities of the corresponding modes, the spectra using a polariser will be used to determine the peak positions.

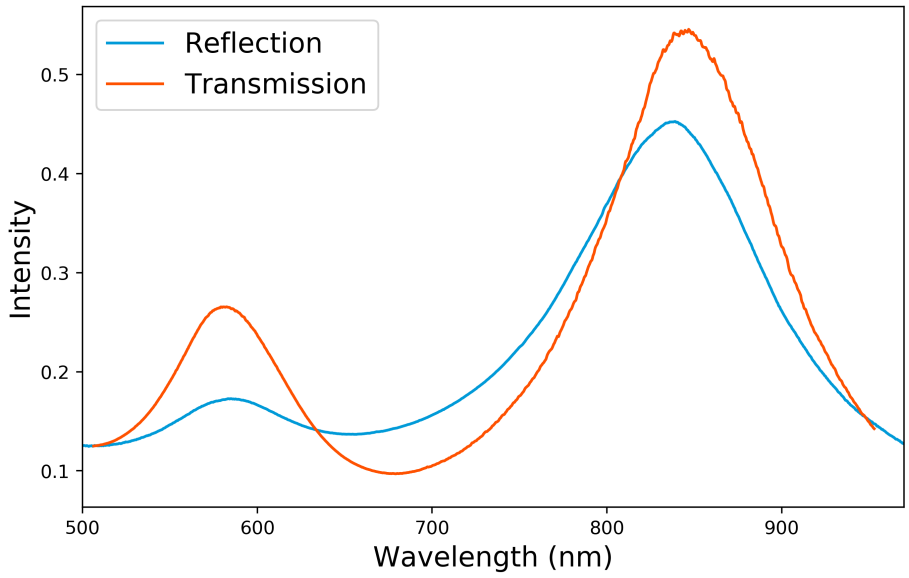

Figure 33: Direct comparison of reflection and transmission. For the transmission spectra, the extinction E = ln(1/T) is shown. The difference in the position of the parallel mode can be seen. The transmission spectrum depicts a stronger contrast of the peaks.

A direct comparison of reflection and transmission is shown in figure 33. The array with 210nm rods was chosen. For the transmission spectrum, the extinction has been plotted to ease the direct comparison. It is well visible that for transmission, the maximum peak intensities surpass the reflection spectrum, while the minimum between the peaks

is also lower. This results in a higher contrast in the transmission spectrum compared to reflection. It should also be noted that the parallel peak position between the two spectra is slightly shifted. Both of these effects will be discussed later on. Furthermore, at the peak of the parallel mode in transmission, a certain roughness is visible which is not present in reflection. This is caused by the LDLS light source used for transmission: The characteristic xenon peaks can still be detected, whereas the purely thermal light source used for reflection depicts no such peaks.

6.1.2 Spectra using polarised light

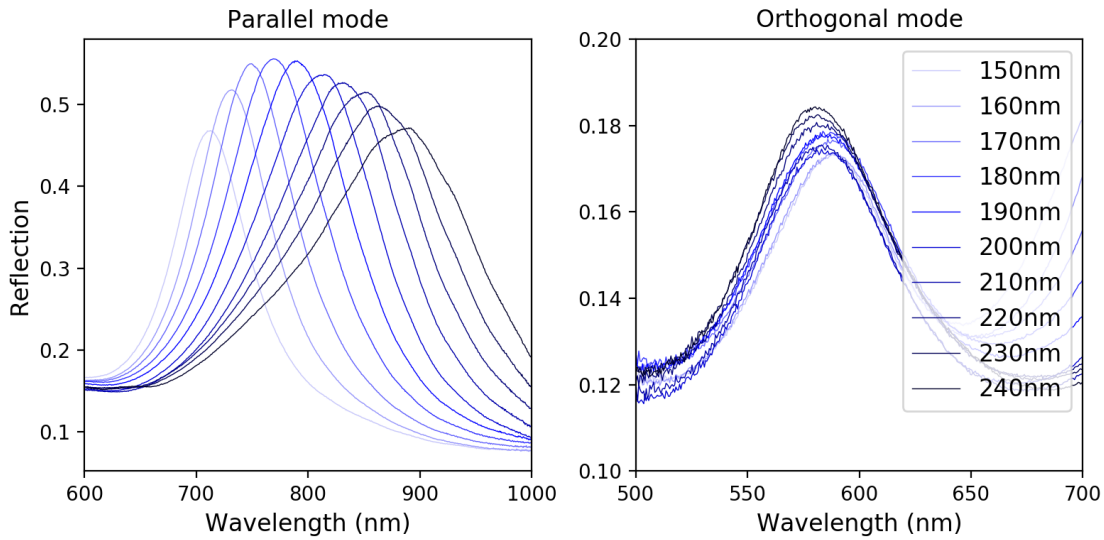

Figure 34: Rod arrays in brightfield in transmission, using polarised light to only excite either the parallel (left) or perpendicular (right) mode.

In figure 34, the individual excitation modes are shown. Polarised light was used to excite them specifically, and the exact peak positions for each spectrum were determined using the centroid. Again, even with polarised light, the amplitudes still do not increase linearly. However, it is visible how the parallel mode redshifts for longer rods, while the perpendicular mode blueshifts slightly. This behaviour was also visible in transmission.

To compare the actual spectral positions of the resonances in transmission and reflection, they have both been plotted in figure 35. A good agreement in the spectral positions of the peaks can be seen. However, in the data for the parallel mode, the peak position in reflection is consistently lower than in transmission, with an average deviation of 15.7nm. This is due to the differences in measuring geometry: In transmission, the incident light minus the absorbed light and a portion of the scattered light is detected. In reflection, only

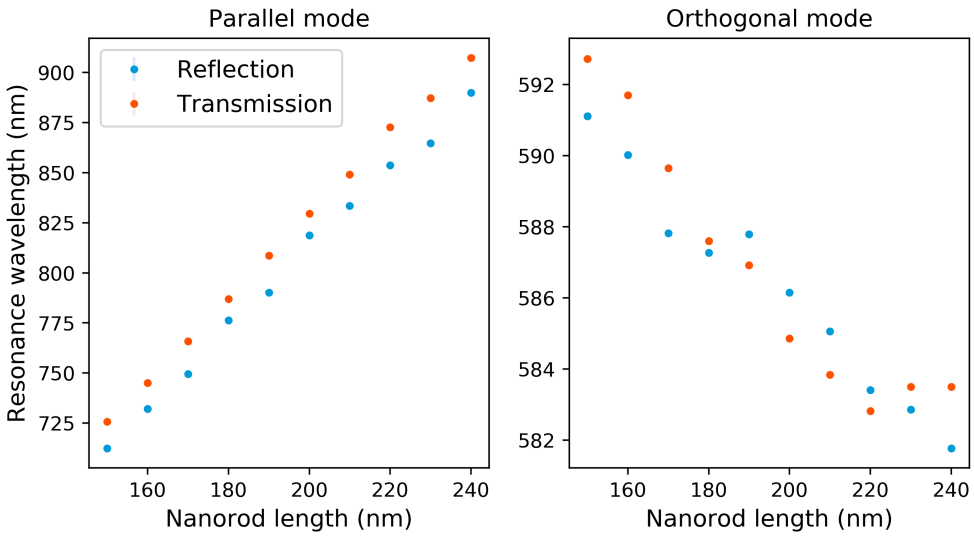

Figure 35: Spectral positions of the parallel (left) or perpendicular (right) mode for different rod lengths. In blue, the data from reflection measurements are shown, in orange the data of the transmission measurements is depicted.

the backscattered light is observed. Since in transmission, both absorption and scattering together cause the spectrum, a slightly different peak position than for pure backscattering may be detected (see [3]).
The spectral positions for the orthogonal mode differ less. The average difference is 1.2nm, and the offset seems somewhat randomly distributed.
It should be noted that the parallel mode was present in every tested polariser position. It did decrease in amplitude, but still always dominated the perpendicular mode in amplitude. The cause for this is unknown.

6.2 Darkfield mode

In addition to the bright field measurements, darkfield spectra of the single structures on the DF-01 sample were taken to compare them to the transmission setup. Since in darkfield mode, only the scattered light is picked up, the overall shape is the same for both reflection and transmission geometry.

The spectra of the disks can be seen in figure 36. The 60nm disks were not bright enough to be detectable. In general, even the other disks display a weak signal, which is most likely due to the structures being manufactured on a transparent substrate which is not ideal for reflection. Reflection of the incident light on the glass surface of the substrate creates a higher background brightness and therefore decreases the contrast

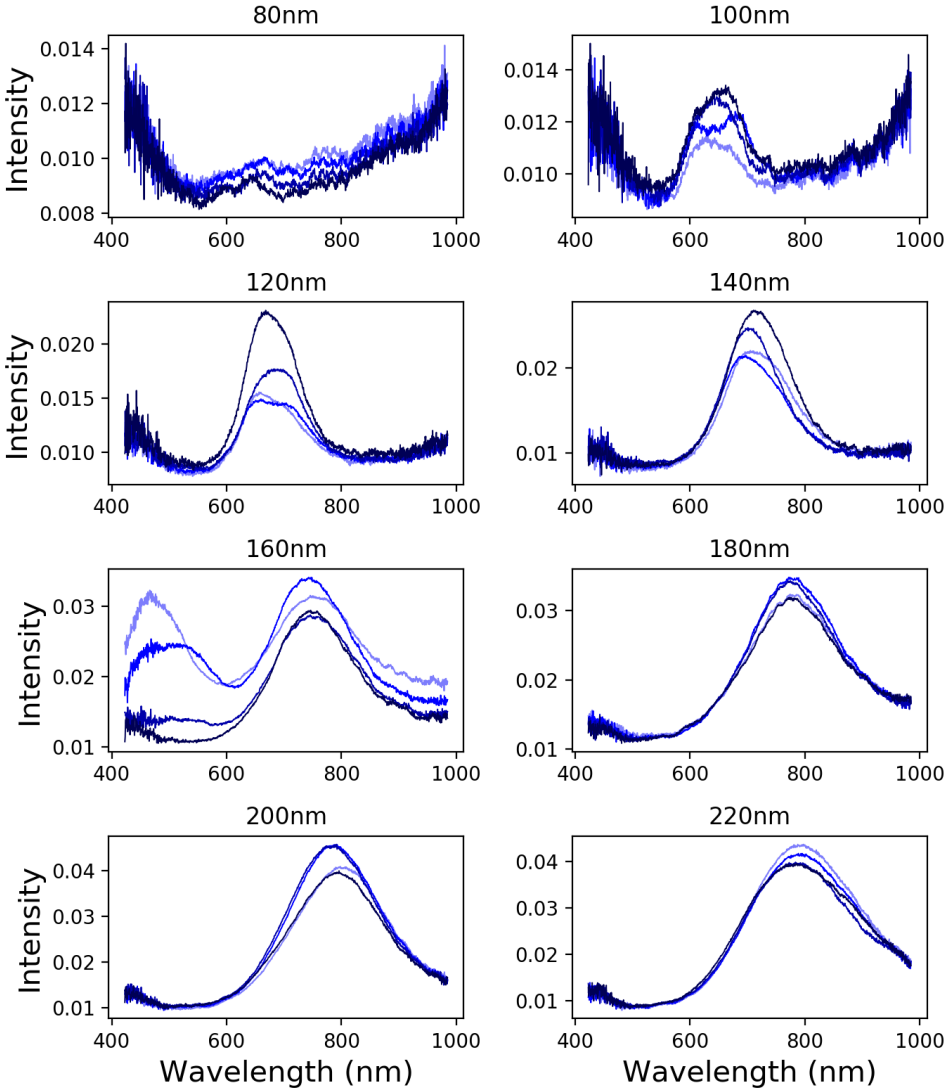

Figure 36: Darkfield reflection spectra of nanodisks. Per size, four different particles are shown. Please note the y-axis: Even for the brightest structures, the background reaches 25% of the peak intensity.

of the particle resonances. Since a purely thermal light source was used here, there are no characteristic lines are visible in any of the spectra. Otherwise, the spectra look as expected. A single resonance can be seen, the spectral positions of which increases with the disk diameter. The disks of 160nm diameter depict a second peak towards the shorter wavelength range, which is caused by a highly radiant imperfection, like dust, close to the structures.
The same measurement was done for the single rods.

In the spectra of the rods, shown in figure 37, only a single resonance is visible. Since unpolarised light was used in these measurements, this is rather unexpected, since the perpendicular mode around 580nm is not present in any of the spectra, while the parallel mode is well pronounced.

A direct comparison of the darkfield spectra in reflection and transmission for disks with a 140nm diameter is shown in figure 38. The differences in peak amplitude and background intensity can be seen: The transmission spectrum displays a higher peak intensity and a lower background than the transmission spectrum. Had the sample been manufactured onto a substrate suitable for reflection, the difference in the background intensity may not be as significant. Like in the brightfield case, due to the different light sources, the xenon lines are visible in the transmission spectrum. Again, like previously, the spectral positions of the transmission and reflection measurements were plotted in the same diagram to allow for an easy comparison. Due to the orthogonal mode not being present in the rod spectra, it could not be used in the comparison.

This diagram is shown in figure 39. On the left, the parallel resonances of the nanorods have been plotted, on the right the disk resonances can be seen.
The spectral positions of the parallel rod modes agree very well. The overall behaviour is identical, and the average difference between reflection and transmission is around 13.2nm. There is however not a constant offset as was present in the brightfield measurements. For the disks, the offset is larger with an average of 24.8nm. The peaks in reflection seem to be blueshifted relative to transmission.

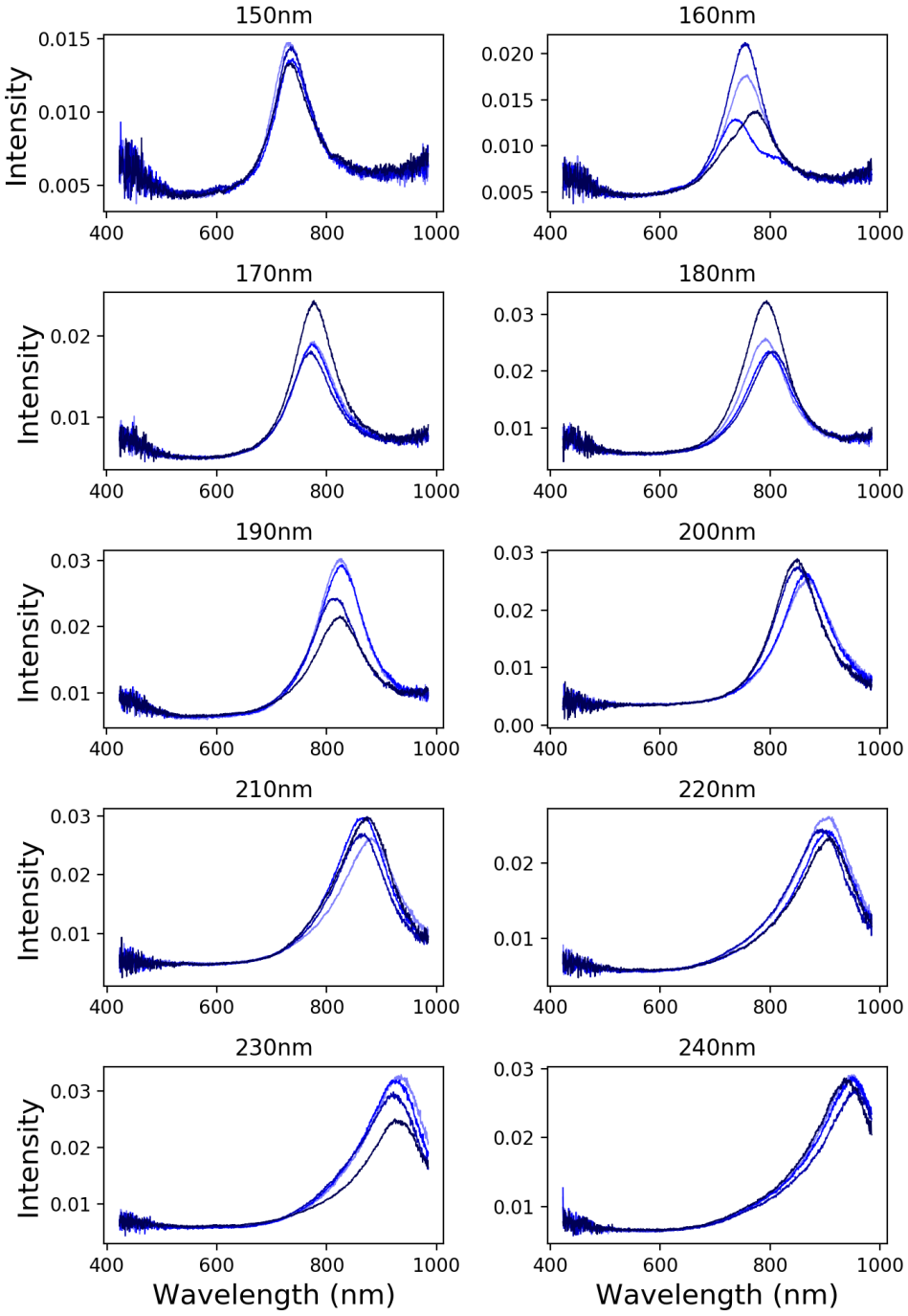

Figure 37: Darkfield reflection spectra of nanorods. The orthogonal modes are not visible on any of the spectra, even though unpolarised light was used. For each size, four particles were measured.

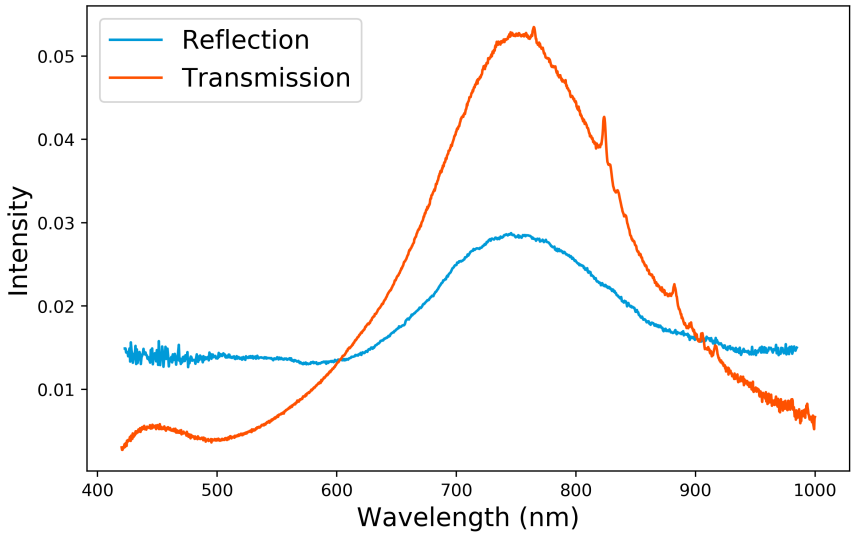

Figure 38: Direct comparison of reflection and transmission for darkfield mode. The higher intensity of the transmission spectrum is well visible. The higher background intensity of the reflection measurement also becomes apparent.

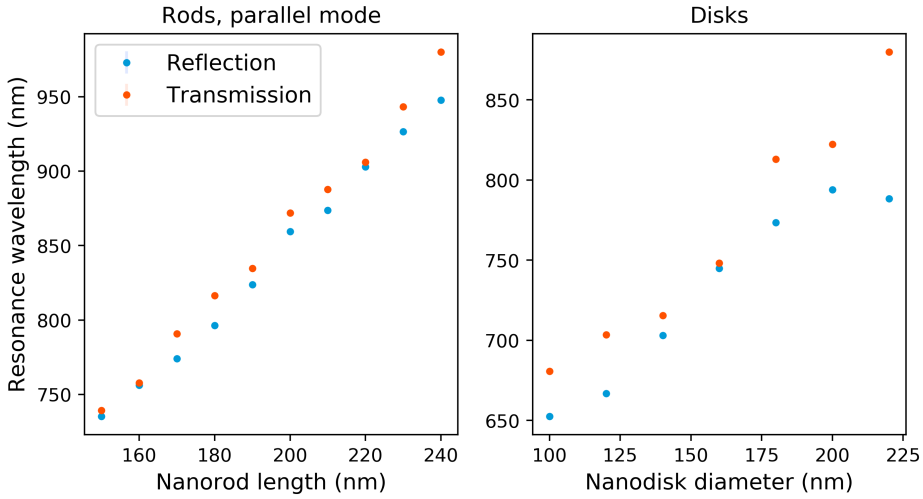

Figure 39: Comparison of the peak positions of the darkfield spectra in reflection (orange) and transmission (blue). On the left, the parallel rod resonances are shown, on the right the disk resonances are depicted. The overall behaviour agrees well, the average difference is 13.2nm for the rods and 24.8nm for the disks.

7 Phase transitioning nanoparticles

To investigate the sample's phase transitioning, the use of the gas cell and gas control system were necessary. As such, the measurements presented here also served as first tests on the functionality and operation of these devices.

7.1 Original state

Before any phase change was induced, the arrays on the DF-02 sample were measured using unpolarised light and brightfield mode. In its original, metallic form, the magnesium structures display plasmonic resonances.

The spectra of the nanorods are shown in figure 40. Since unpolarised light is used, both the parallel and perpendicular modes are excited and visible. In comparison to the gold sample, the peaks are not as well pronounced and separated: Due to the superimposed peaks, the weaker orthogonal resonances of the shorter rods appear as plateaus rather than distinct peaks. This has led to problems in determining the exact peak positions, which could have been circumvented by using polarised light. With increasing rod length, the peak intensity and distance between them increase, making them more pronounced. The problem of fitting therefore only affects the shorter rods. The spectra also

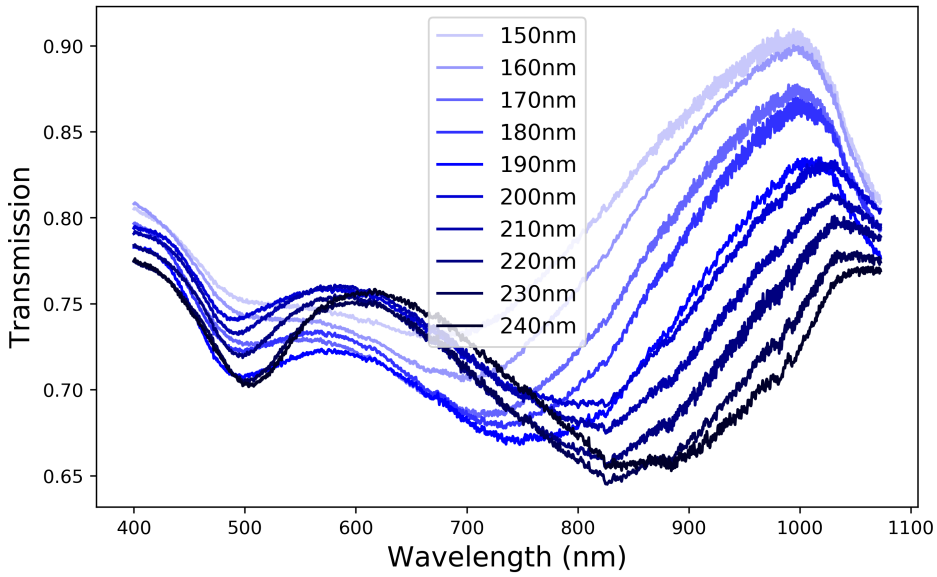

Figure 40: Spectra of all rod arrays on the DF-02 sample. The two superimposed peaks are visible, but not as well as on the gold sample. The peaks are blueshifted compared to gold.

appear more noisy than the spectra of the gold nanostructures of the same dimensions. This is most likely due to noise introduced by the glass windows of the gas cell in which the sample was kept during the measurements. The gas cell requires a specific size of windows which had to be custom made. Until these dedicated glass windows were delivered, unsuited and oversized glass was used temporarily, which caused the noise visible in these spectra.

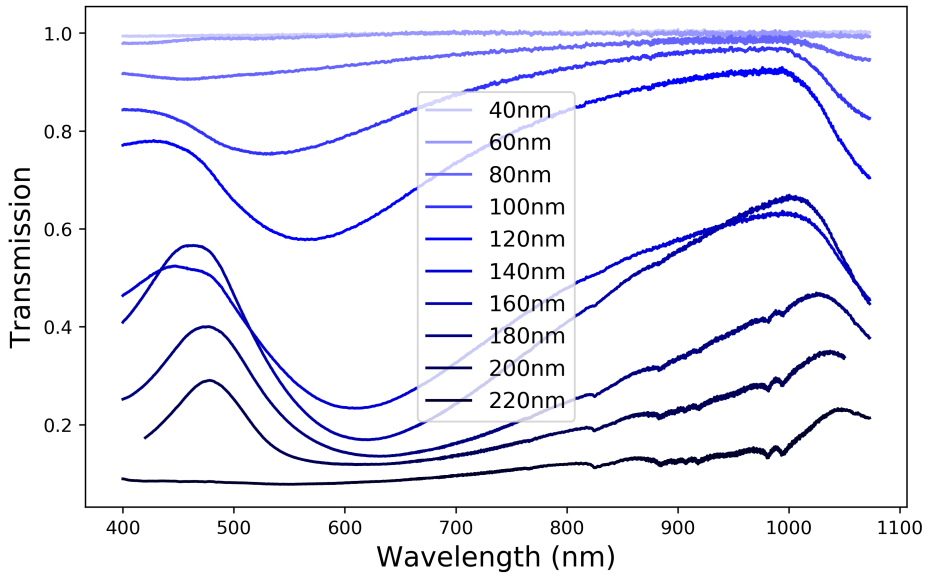

Figure 41: Spectra of all disk arrays on the DF-02 sample. The first arrays are extremely weak due to the small particle sizes.

The spectra of the nanodisks can be seen in figure 41. The first three spectra display no noticeable resonance and a very small overall extinction, which is caused by the very low coverage in the arrays with small disks. For the largest disks, the transmission is very low and again, no peak is visible. Based on what happened to the gold disks, this is most likely due to the large disks growing into each other, resulting in a full coverage of the array with a solid film rather than nanoparticles. Overall, the increasing extinction of the disks with increasing size is well visible, mostly caused by the increasing coverage. Due to slight non-linearity of the CCD sensor, the xenon peaks in the LDLS spectrum become visible in the spectra of lower transmission. It should also be noted that the 200nm disks do also display a considerably wide and somewhat distorted dip, which might also indicate some damage.

Again, where possible, the peak positions were determined by calculation of the centroid and plotted over the characteristic structure size. For both modes of the rods this

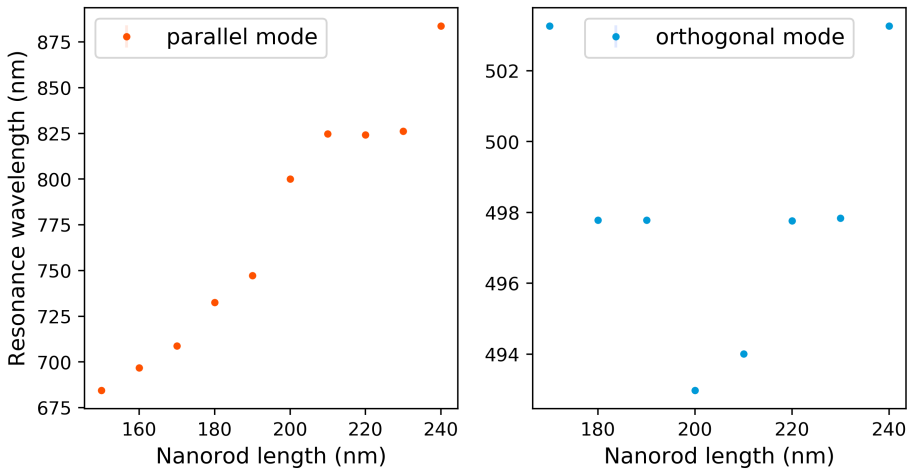

Figure 42: Shift of the spectral positions of the parallel (left) and orthogonal mode (right) of the magnesium nanorods. The blueshift compared to gold is around 44.9nm for the parallel mode and around 87.3nm for the orthogonal mode.

can be seen in figure 42. Overall, the behaviour of the spectral peak position on the rod length is not clear as for the gold particles. For the parallel mode, deviations from the expected linear behaviour are much greater. In case of the orthogonal mode, an entirely different nature of the values can be seen: There seems to be a minimum at a rod length of 200nm. The fluctuations seen here are most likely the cause of the degradation of magnesium nanostructures by oxygen and moisture as well as carbon dioxide in the atmosphere. Due to its reactivity, magnesium is in general a more difficult material to work with compared to the inert gold. The fact that layers of different metals were used here may also effect the resonances.
It is also noticeable that the resonances for rods of the same dimensions are at shorter wavelengths for magnesium compared to gold. On average, the parallel resonances are blueshifted by 44.9nm, and the perpendicular resonances are at wavelengths 87.3nm shorter. This is the result of the different dielectric functions of magnesium and gold (see equations 39,47).

Since all disk arrays were manufactured on the DF-02 sample, their peak shifts were also analysed. The plot of spectral peak position versus disk diameter can be seen in figure 43. Only for disk diameters of 80nm to 200nm there was a peak to be fitted, the smaller disks and the one larger array did not display a significant dip in the transmission spectra. Since the dip of the 200nm disks seems rather distorted, it is not surprising that

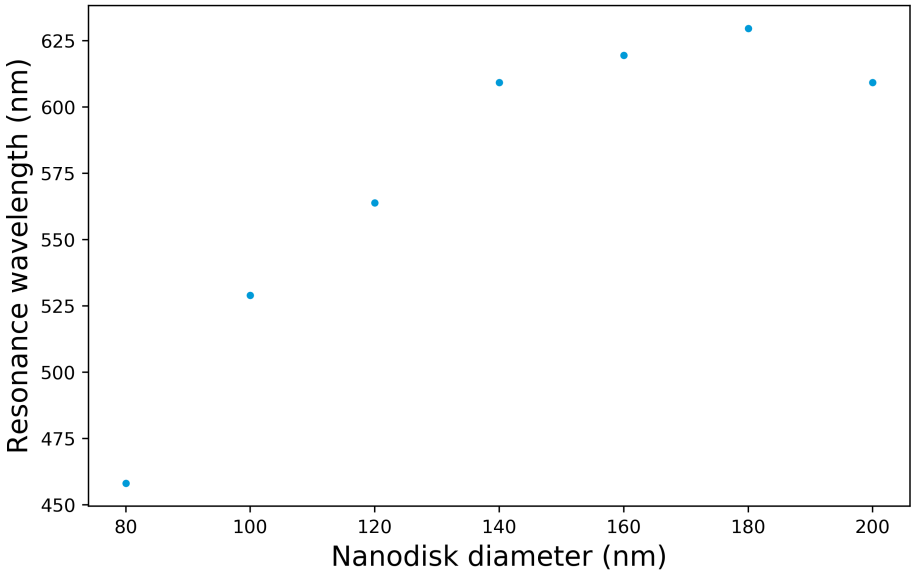

Figure 43: Shift of the spectral positions of the resonances of the magnesium nanodisks.

it does not conform to the expected redshift in the peak position with increasing disk size. Other than that, the spectral positions increase with the disk diameter, as Gans-theory indicates.

7.2 Brightfield measurement of phase transition

The phase transitioning properties of the DF-02 sample were investigated using bright field measurements on the arrays on the sample. The measurements began by taking spectra of all arrays on the sample using unpolarised light, while flowing nitrogen (1 ln/min). Thereafter, spectra of the rod array with rod length of 230nm were measured repeatedly while exposing the sample to 10% H_2 in N_2 to induce the phase transition to the dielectric dihydride. Once saturation was reached, all arrays have been measured again, before exposing the sample to 20% O_2 in N_2 to revert the process and restore the structures to their original metallic state. Like before, during the exposure to oxygen, the 230nm rod array was repeatedly measured. For some of the arrays, the bright field spectrum was remeasured the day after the experiment, as well as 5 days later.

For a two of the rod arrays and two of the disk arrays, the spectra before and after the gas exposure are shown in figure 44. If the spectrum of an array was remeasured a day and 5 days after the hydrogen exposure ended, the spectra are also shown.

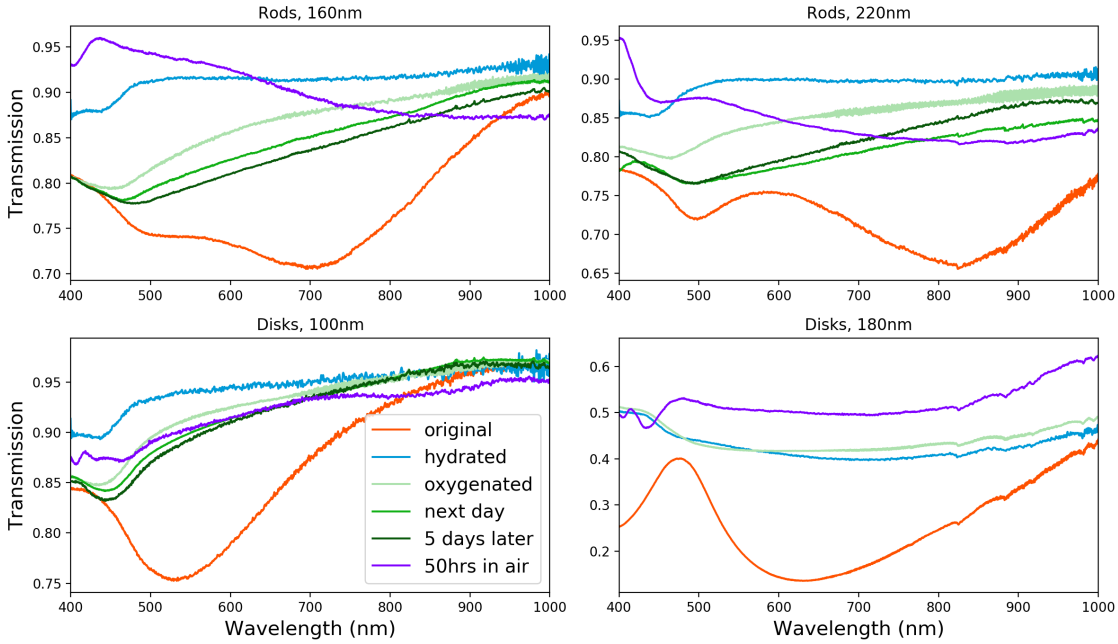

Figure 44: Bright field measurements on some of the arrays on the DF-02 magnesium sample. Depicted are original spectrum (orange), hydrogenated (blue), and after oxygen exposure (light green). The resonance peaks in the original spectra are well visible, and it can clearly by seen how no resonances are present after hydrogenation. Ideally, after exposure to oxygen the spectrum would return to its original shape. Even after 5 days in vacuum and 50 hours of exposure to ambient air, this does not happen. If not stated otherwise, the samples were stored in a vacuum.

Towards longer wavelengths, increasing noise can be seen in the spectra. This was caused by the cover glass used as windows for the gas cell, which were used as a temporary solution until the dedicated Schott glass windows were delivered.

Hydrogenation

Upon exposure to 10% hyrogen in nitrogen, the phase transition to dielectric magnesium dihydride was successfully induced, as can be seen from the increasing transmission and disappearance of the resonances in the blue spectra (figure 44), which were taken after the hydrogenation. The maximum transmission reached for each array is limited by the coverage of structures, as such more densely packed arrays have a lower maximum transmission, even after hydrogen exposure. While in the original state, noticeable resonance peaks can be seen in the spectra, the transmission after hydrogen exposure is largely flat and homogeneous, from a wavelength range of 450nm to more than 1000nm. High amounts of noise can be seen in some of the spectra towards longer wavelengths, these are caused by the glass used in the gas cell.

To further investigate the process of hydrogenation, the transmission at 825nm of the 230nm rod array was plotted during the hydrogenation process in figure 45. The wavelength was chosen since it roughly represents the parallel mode resonance of the array, and thus a particularly large shift in transmission during hydrogenation is possible. As expected, a large increase in transmission can be seen as the phase transition of the magnesium progresses. From original state to saturated state after hydrogenation, the transmission changes from 65% to 90%, representing a 38% increase. Since noticeable noise appeared during the measurements, it was paused to check for the cause and then later resumed. From the flat behaviour towards the end, it can be assumed that the structures reached saturation after around 90 minutes, and exposure to hydrogen was stopped after roughly two hours. Then, all arrays were measured again (figure 44).

Dehydrogenation

To revert the magnesium dihydride back to metallic magnesium, exposure to oxygen is used. Ideally, if the phase transition could be fully reversed, the spectra of the arrays after oxidisation (light green) would be identical to the original spectra (orange) in figure 44. This did however not fully occur, after oxidisation the spectra only reach a position somewhere between hydrated and original state, and the resonances do not reappear with noticeable magnitude. After the actual experiment, the sample was stored away in a desiccator under vacuum, and some of the arrays were remeasured the next day and five days later, to see if any further changes occur. After multiple days the spectrum did shift slightly further towards its original shape, but not severely enough to restore the

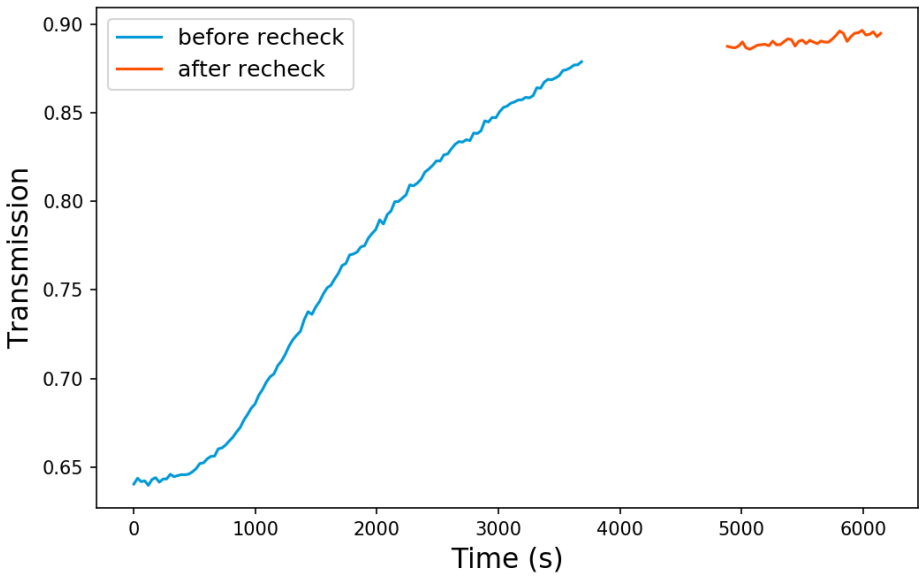

Figure 45: Transmission of the 230nm rod array during hydrogenation at a wavelength of 825nm, which is roughly at the position of the parallel resonance. Therefore, if the material transitions to its dielectric state, the transmission at this wavelength will increase significantly as the resonances disappear. This can clearly be seen. Since excessive noise appeared in the measurement, it was paused and later resumed, indicated by the two differently coloured parts of the curve.

resonances.

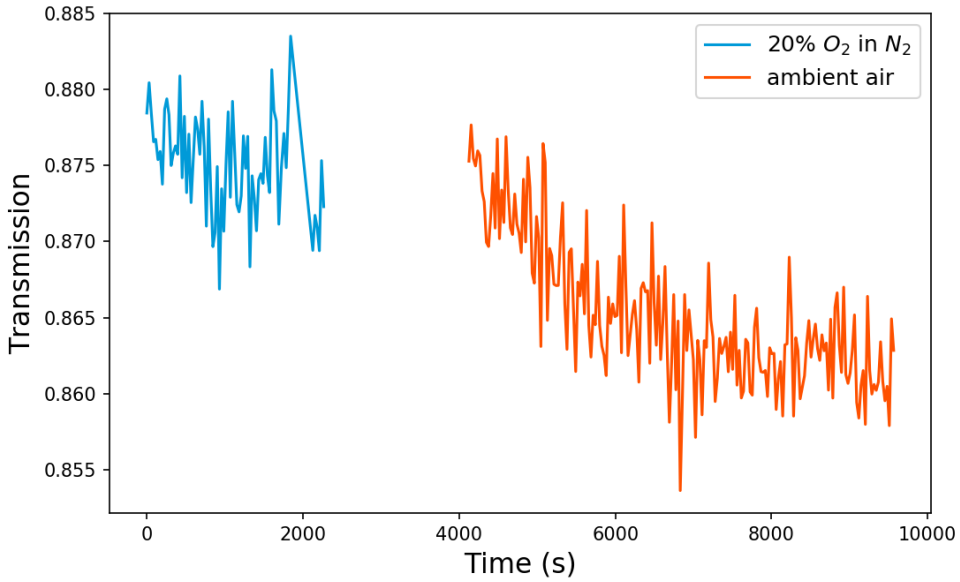

Figure 46: Transmission of the 230nm rod array during oxidisation at a wavelength of 825nm. The transmission is supposed to decrease as the dielectric magnesium dihydride reverts back to metallic magnesium. A slight decrease can be seen, but not nearly as strong as upon hydrogenation. Due to technical problems, the use of oxygen from the gas system had to stop, and ambient air was used for the rest of the exposure.

As during hydrogenation, the transmission of the 230nm rod array at 825nm wavelength was monitored during oxygen exposure. This is shown in figure 46, and a slight decrease in transmission is indeed visible. The process is however much slower, and the original transmission is not reached.

The restoration of the structures to their fully metallic state did therefore not succeed, only partial restoration was achieved. This is believed to be caused by impurities in the magnesium due to contaminants in the evaporator which was used to create the metal layers.

Second attempts were made to manufacture a functional magnesium sample by doing the evaporation in an ultra high vacuum chamber. During these attempts, a magnesium film and a second structured sample were manufactured. They both displayed the same problem as the sample discussed above: the hydrogenation of the material worked, despite being slower than expected. The dehydrogenation did not work, even after multiple hours of exposure to oxygen the optical properties before hydrogen loading could not be

restored. In addition to this, the lift-off on the structured sample did not work properly, resulting in only two usable disk arrays. Since no new information was gathered from these samples, they have not been presented in this thesis.

8 Discussion, Conclusion and Outlook

In this thesis, a newly installed experimental setup for both brightfield and darkfield optical microscopy in transmission was tested to ensure all components work as expected. The setup consists of an inverted microscope with magnifications of x4, x10, x20 and x60, and condensers for both brightfield and darkfield application. A grating spectrometer with a CCD sensor is attached to the microscope and allows for spectroscopy in the entire visible spectrum. A gas system with four mass flow controllers can be used to precisely control four gasses at the same time, which is crucial for the research of phase transitioning nanoparticles. A custom gas cell was designed to work in conjunction with the gas system and microscope, to allow in-situ measurements during hydrogenation and dehydrogenation of samples.

To check the functionality of the setup, two samples were used. On each of the samples, nanodisks and nanorods of various sizes and diameters were manufactured in densely packed arrays for brightfield and more scarcely as single structures for darkfield microscopy. The first sample was made of gold on an ITO/glass substrate, since gold is a well-understood and stable material for nanotechnology. The second sample was constructed of a Ti/Mg/Ti/Pd sandwich on an ITO/glass substrate. These magnesium nanostructures can phase transition to non-metallic magnesium dihydride, and thus served to verify the functionality of the gas system and gas cell.
The first measurements were used to determine the characteristics of the new setup. Those included the spectrum of the laser driven light source, the usable spectral range of the spectrometer, relative transmission and orientation of the polariser, as well as the long-term stability of the light source. The usable spectral range was measured to be between 350nm and 1050nm, being limited by the absorption of the glass optics and the second order of diffraction. The polariser in the setup transmits mostly evenly, except for significant absorption around 450nm.
After a 30 minute warm up time, the intensity of the light source fluctuates less than 0.6% and is ready to be used for measurements.
Using the DF-01 gold sample, the brightfield and darkfield mode of the microscope were first tested. Sadly, most of the disk arrays were either not manufactured or severely damaged, so that most of the data analysis had to focus on the rod arrays. All spectra were smooth, and the peaks were well pronounced. By calculating the centroids of the dips for all resonances, their spectral positions could be determined and compared to theoretical results. Since Gans-theory for spheroids was used to approximate the rods and disks on the sample, a value-by-value comparison is not useful, numerical simulations would be necessary for such a direct comparison. Nonetheless, the overall behaviour of

the spectral positions of the resonances agree well with the analytical theoretical models. The darkfield measurements were also smooth and well pronounced. Due to the longer distance between the particles, they can no longer couple, which causes a slight shift in the spectral positions of all the peaks.

To compare the new setup to another, similar experiment, the DF-01 sample was re-measured in a reflection microscope for spectroscopy in the visible range at the MPI IS in Stuttgart. By design, the substrate of the DF-01 sample is not ideal for reflection microscopy. Ideally, such samples are manufactured onto an absorbing substrate such as silicon, opposed to the transparent ITO/glass substrate used for transmission samples. Nonetheless, both brightfield and darkfield spectra of the DF-01 sample could be measured. In brightfield mode, due to the nature of reflection, the spectra have a low background with high-amplitude peaks at the resonances, whereas in transmission the spectra feature a high background with low-intensity dips at the resonance wavelengths. The peak positions were determined by calculating the centroid just like before and compared to the transmission measurements. An average, almost constant offset of 15.7nm for the parallel mode and a more statistically distributed difference of 1.2nm in the perpendicular mode could be seen. The differences are most likely caused by the different geometries used for the measurements.

In the darkfield mode, the perpendicular modes of the rods did not appear on any of the spectra, even though unpolarised light was used. Other than that, the spectra resembled the ones measured in transmission. Again, the spectral positions of the peaks were compared. The differences were an average of 13.2nm for the parallel rod mode, and 24.8nm in case of the disks.

Comparing the intensities of reflection and transmission is not strictly possible, since the unsuitable substrate for reflection decreases the amplitudes. Overall, the results from the two microscopes agree well with one another.

The phase transitioning of the magnesium nanostructures did not fully succeed. The hydrogenation, resulting in a loss of plasmonic activity, did work, but took about 100 minutes, and thus about ten times as long as was reported by Florian Sterl et al ([7]). The attempt to restore plasmonic activity by dehydrating the particles and reverting them back to metallic magnesium did not succeed, even after more than 2.5 hours of exposure to 20% O_2 in N_2. Even attempts to restore the structures by storing them in air for 50 hours did not restore any further activity.

However, both the gas cell and gas system were tested and functioned as expected. The ability of the gas cell to work with any objective and condenser of the microscope was successfully demonstrated.

Acknowledgement

I would like to thank Prof. Dr. Laura Na Liu for the opportunity to do my thesis in her research group, as well as Prof. Dr. Annemarie Pucci for the co-examination. I am very grateful for all the advice and the supervision of my thesis by Dr. Frank Neubrech. I would also like to thank Dr. Ping Yu for the manufacture of the DF-01 and DF-02 samples as well as Marcus Matuschek for his advice on the thesis. Furthermore, i would like to thank Felix Scherz and Anton Kompatscher for the production of a magnesium thin film. At last, i would like to thank all other group members for their support, the Python programming community for their help in all questions regarding data processing, and George M. Rapata for the invention of cable ties.

References

[1] Zayats, A. V., Smolyaninov, I. I., Maradudin, A. A. (2005). Nano-optics of surface plasmon polaritons. Physics Reports, 408(3–4), 131–314. https://doi.org/10.1016/j.physrep.2004.11.001

[2] Mie, Gustav, (1908). Beiträge zur Optik trüber Medien, speziell kolloidaler Metallösungen. Annalen Der Physik, 330(3), 377–445. https://doi.org/10.1002/andp.19083300302

[3] Quinten, M. (2011). Optical Properties of Nanoparticle Systems : Mie and Beyond (4th ed.). John Wiley & Sons, Incorporated.

[4] Gans, R. (1912). Über die Form ultramikroskopischer Silberteilchen. Annalen Der Physik, 352(10), 270–284. https://doi.org/10.1002/andp.19153521006

[5] Maier, S. A. (2007). Plasmonics: Fundamentals and Applications. New York, NY: Springer US. https://doi.org/10.1007/0-387-37825-1

[6] Bohren, C. F., & Huffman, D. R. (Eds.). (1998). Absorption and Scattering of Light by Small Particles. Weinheim, Germany: Wiley-VCH Verlag GmbH. https://doi.org/10.1002/9783527618156

[7] Sterl, F., Strohfeldt, N., Walter, R., Griessen, R., Tittl, A., & Giessen, H. (2015). Magnesium as Novel Material for Active Plasmonics in the Visible Wavelength Range. Nano Letters, 15(12), 7949–7955. https://doi.org/10.1021/acs.nanolett.5b03029

[8] Christy L. Haynes, Adam D. McFarland, LinLin Zhao et al. (2003). Nanoparticle Optics: The Importance of Radiative Dipole Coupling in Two-Dimensional Nanoparticle Arrays†. https://doi.org/10.1021/JP034234R

[9] Sterl, F., Linnenbank, H., Steinle, T., Mörz, F., Strohfeldt, N., & Giessen, H. (2018). Nanoscale Hydrogenography on Single Magnesium Nanoparticles. Nano Letters, 18(7), 4293–4302. https://doi.org/10.1021/acs.nanolett.8b01277

[10] Ranjan, M. (2013). Predicting plasmonic coupling with Mie-Gans theory in silver nanoparticle arrays. Journal of Nanoparticle Research, 15(9). https://doi.org/10.1007/s11051-013-1908-7

[11] Maradudin, A. A., & Leskova, T. A. (2010). Transformation of surface plasmon polaritons by surface structures. Physica B: Condensed Matter, 405(14), 2972–2977. https://doi.org/10.1016/j.physb.2010.01.016

Erklärung / Declaration

Ich versichere, dass ich diese Arbeit selbstständig verfasst und keine anderen als die angegebenen Quellen und Hilfsmittel benutzt habe.

Ort, Datum

Unterschrift

A Design specifications of the DF-01 sample layout

DF-01

20180312

Samples for testing transmission darkfield

Sample layout

Square
80x80 µm^2

height = 40 nm

Square
80x80 µm^2

Arrays - disks

Arrays - rods

“single” - disks

“single” - rods

For calibration

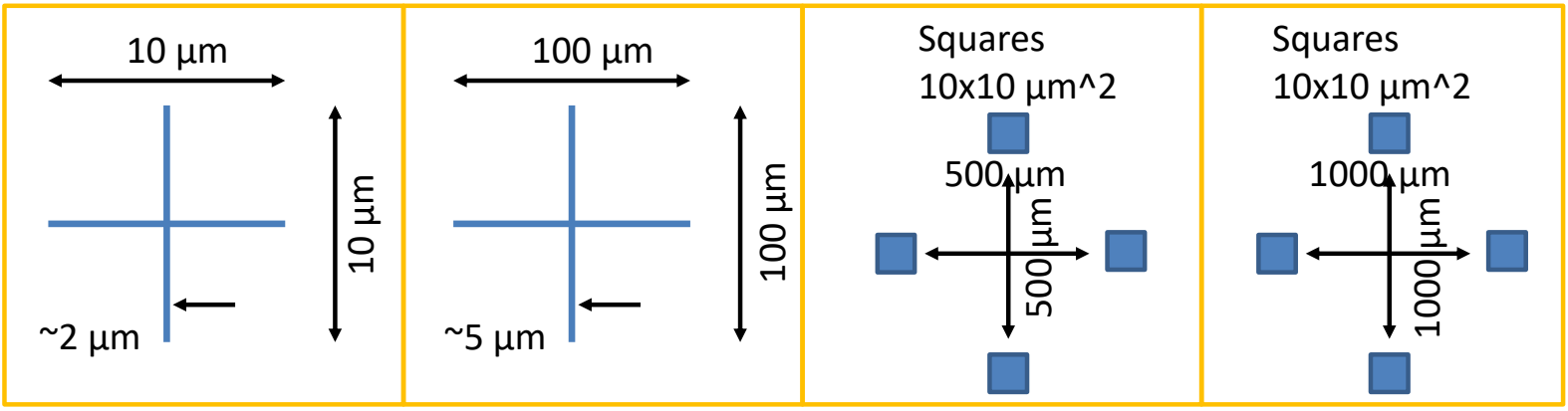

Arrays - disks

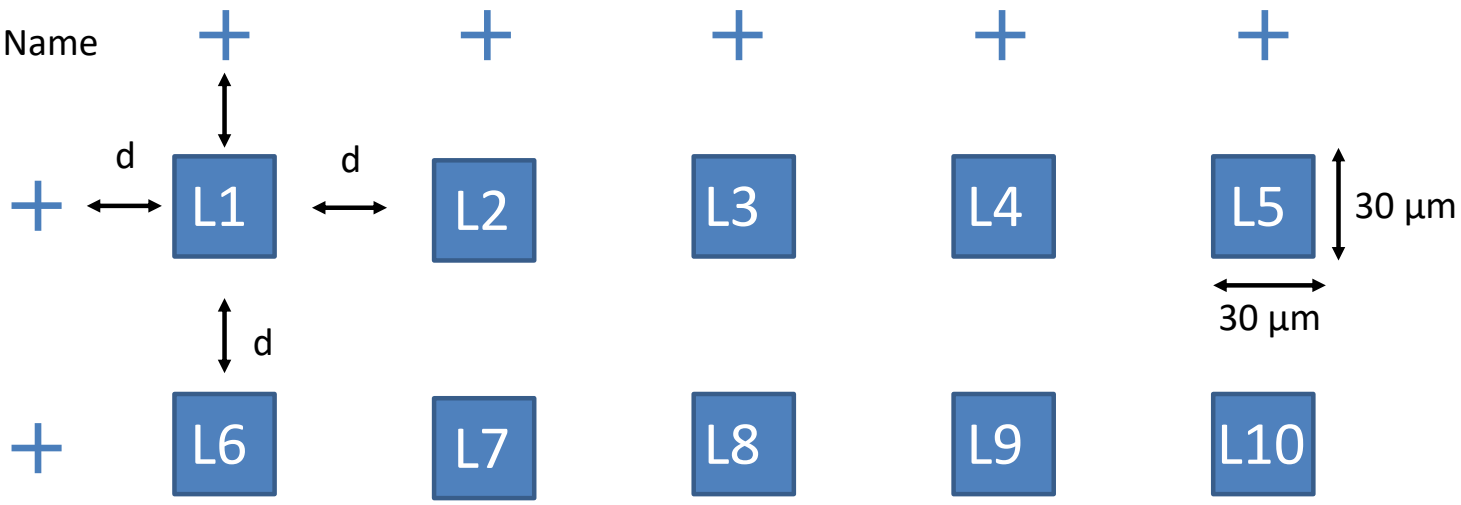

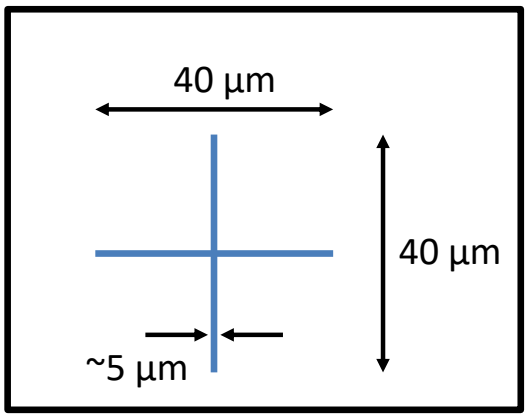

periodicity: p_y = 300 nm

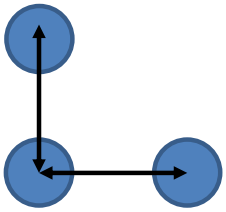

Periodicity: g_x = 300 nm

L1 = 40 nm
L2 = 60 nm
L3 = 80 nm
L4 = 100 nm
L5 = 120 nm
L6 = 140 nm
L7 = 160 nm
L8 = 180 nm
L9 = 200 nm
L10 = 220 nm

Paramter:
d = 70 µm

“Single” - disks

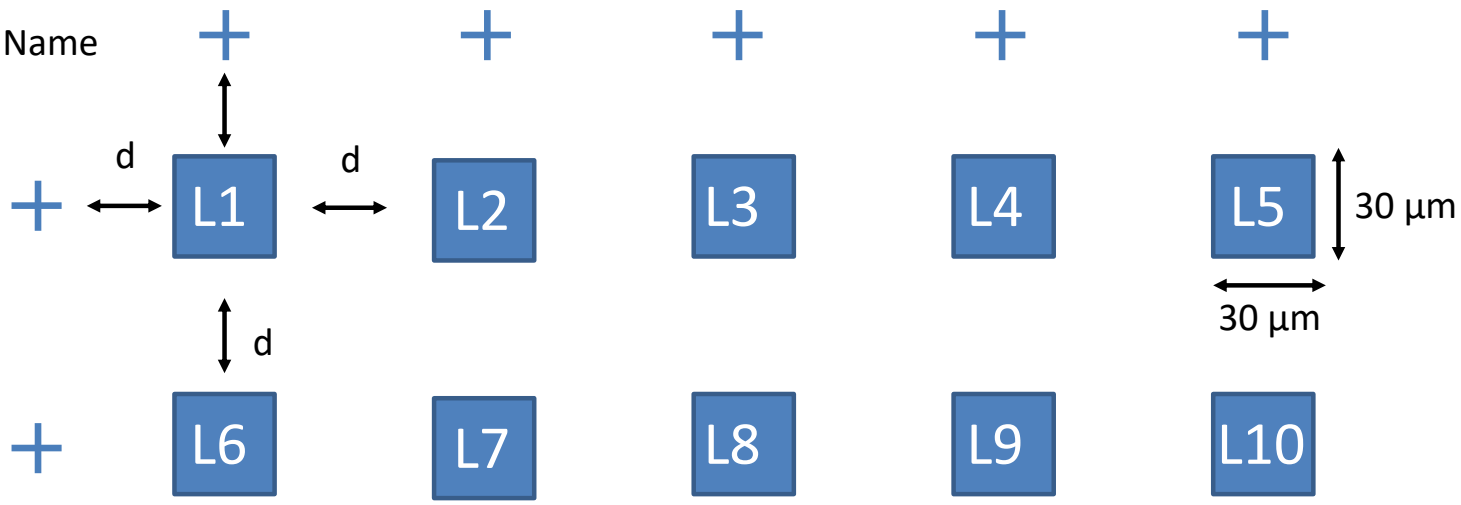

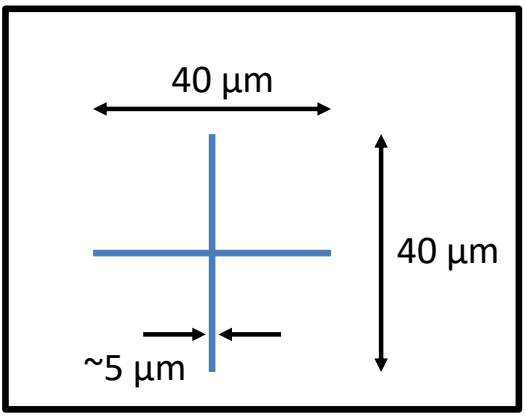

3x3 antennas

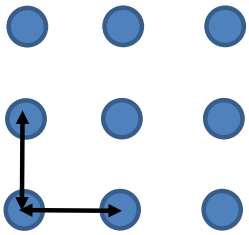

Periodicity: p_y = 10000 nm

Periodicity: p_x = 10000 nm

L1 = 40 nm
L2 = 60 nm
L3 = 80 nm
L4 = 100 nm
L5 = 120 nm
L6 = 140 nm
L7 = 160 nm
L8 = 180 nm
L9 = 200 nm
L10 = 220 nm

Parameter:
d > 60 µm

Arrays - rods

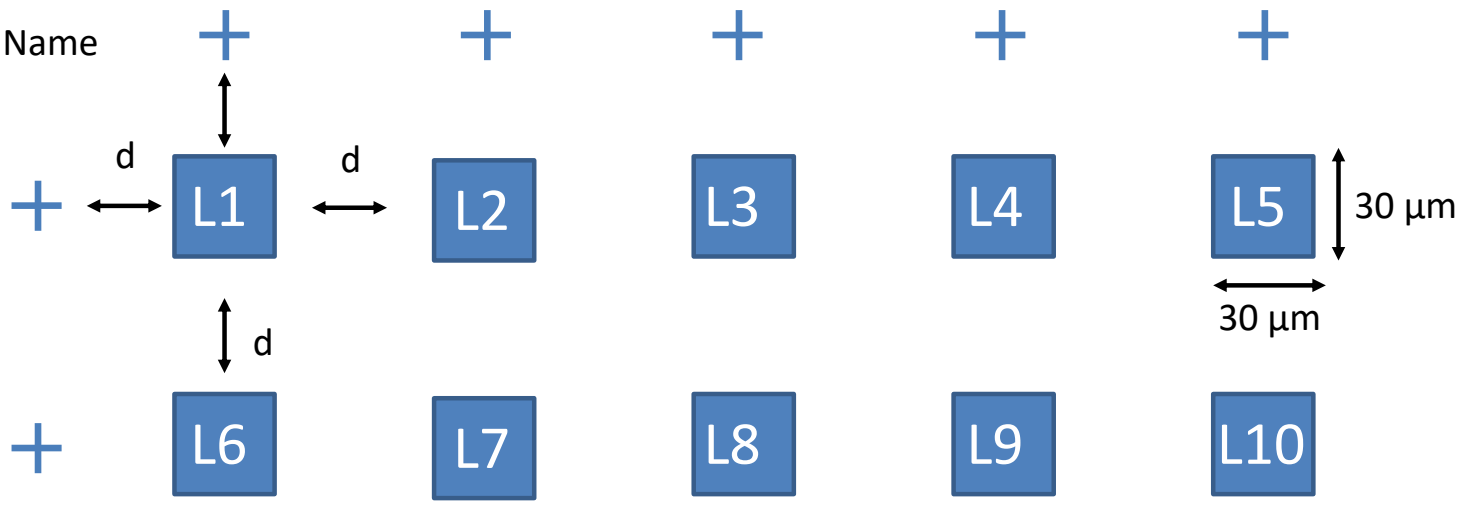

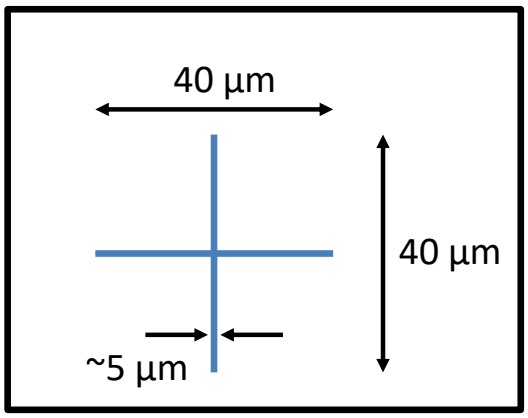

Periodicity: p_y = 300 nm

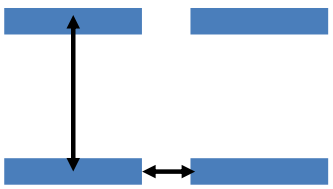

Distance: g_x = 100 nm

L1 = 150 nm
L2 = 160 nm
L3 = 170 nm
L4 = 180 nm
L5 = 190 nm
L6 = 200 nm
L7 = 210 nm
L8 = 220 nm
L9 = 230 nm
L10 = 240 nm

Parameter:
d = 70 µm

Width:
w=60nm

“Single”- rods

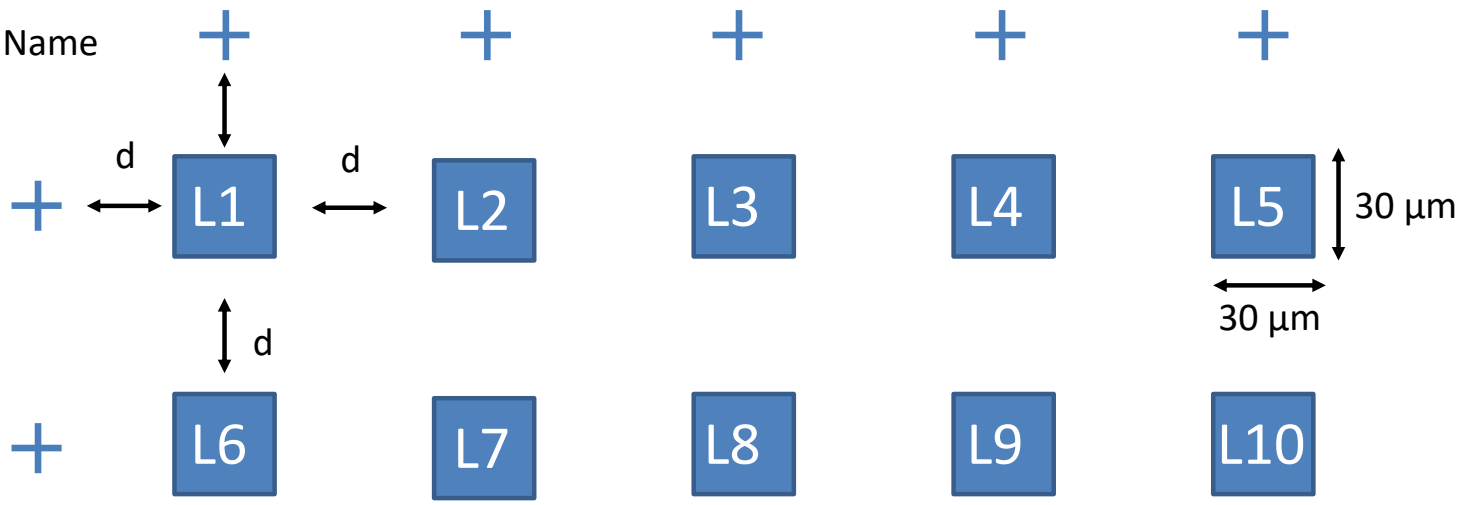

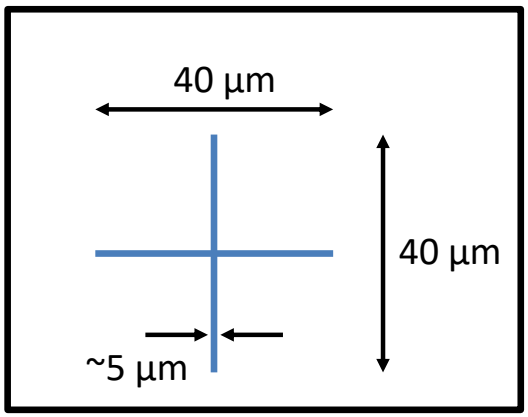

3x3 antennas

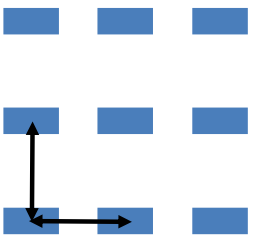

Periodicity: p_y = 10000 nm

Periodicity: p_x = 10000 nm

L1 = 150 nm
L2 = 160 nm
L3 = 170 nm
L4 = 180 nm
L5 = 190 nm
L6 = 200 nm
L7 = 210 nm
L8 = 220 nm
L9 = 230 nm
L10 = 240 nm

Parameter:
d = 70 µm

Width:
w=60nm

B Peak determination by calculating the centroid

There are multiple ways the position of a peak of a set of data points can be determined. The two most commonly used are fitting a function to the data points and using the centroid. In this thesis, the centroid method was used.
The centroid itself is a value similar to a centre of mass: First, the general peak position is determined, and all points in a range around the peak will be used for the centroid calculation. The centroid itself is then calculated by the following equation:

$$x_{\text{centroid}} = \frac{\sum_{x \in S} x \cdot f(x)}{\sum_{x \in S} f(x)} \tag{49}$$

Here, S is the subset of data points x within the predefined range of the peak, and f(x) is the value of a given data point. In the case of spectra like in this thesis, x refers to the spectral position of a point, and f(x) refers to its intensity.

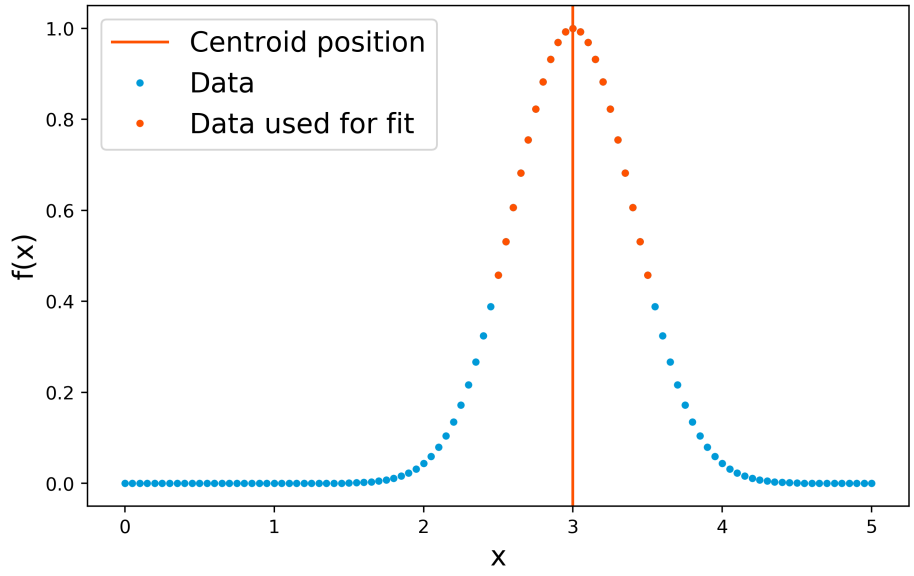

Figure 47: Visualisation of a centroid calculation. In a set of data points (blue), a subset S (orange) of points around the peak is defined. By applying equation eq:centroid to this subset, the centroid (orange vertical line) can be determined.

Figure 47 shows the basic principles of a centroid calculation. The subset around the peak determines the quality of the centroid. More points improve the quality, but points far away from the peak decrease it. Therefore, like all other peak detection tools, the centroid works best for many points densely arranged around the peak.